NASA TECHNICAL NOTE (NASA TN D-3532)

NASA TN D-3532

DESIGN AND COOLING PERFORMANCE OF A DUMP-COOLED ROCKET ENGINE

by Albert J. Pavli, Jerome K. Curley, Philip A. Masters, and R. M. Schwartz

Lewis Research Center
Cleveland, Ohio

NATIONAL AERONAUTICS AND SPACE ADMINISTRATION • WASHINGTON, D. C. • AUGUST 1966

NASA TN D-3532

DESIGN AND COOLING PERFORMANCE OF A DUMP-COOLED ROCKET ENGINE

By Albert J. Pavli, Jerome K. Curley, Philip A. Masters, and R. M. Schwartz

Lewis Research Center
Cleveland, Ohio

NATIONAL AERONAUTICS AND SPACE ADMINISTRATION

For sale by the Clearinghouse for Federal Scientific and Technical Information
Springfield, Virginia 22151 – Price $2.00

DESIGN AND COOLING PERFORMANCE OF A DUMP-COOLED ROCKET ENGINE

by Albert J. Pavli, Jerome K. Curley, Philip A. Masters, and R. M. Schwartz

Lewis Research Center

SUMMARY

A dump-cooled engine was designed and experimentally evaluated as a 500-pound-thrust rocket engine operating at 100-psig chamber pressure with gaseous hydrogen and liquid oxygen as propellants and liquid hydrogen as a coolant. Fourteen firings were made; of these, the last four were with a refractory coating of aluminum oxide on the flame-side surface.

Data showing the measured and analytical heat fluxes along with coolant temperatures and pressures through the engine for various coolant flows are presented as a means of determining the minimum satisfactory coolant flow and of checking the validity of the design technique used. In spite of using the obsolete (and incorrect) combustion gas properties in the design of the coolant passages, it was possible to optimize coolant velocity over the main portion of the chamber and to hold the metal temperatures nearly constant and equal to the material limit. The minimum satisfactory coolant flow for this engine was 6.9 and 7.5 percent of the total propellant flow for the engine with and without the refractory coating, respectively.

The projected potential of dump cooling was investigated by using an analytical performance prediction that assumed a high-temperature inner shell (molybdenum). The results indicated that the coolant exit temperature could be made high enough to yield coolant specific impulses up to and perhaps greater than the specific impulse of the main combustion process.

INTRODUCTION

A theoretically attractive scheme of cooling rocket engines that has been proposed by Rocketdyne (unpublished) is a technique referred to as "dump cooling." This concept of cooling has particular promise when considered for a pressure-fed liquid-propellant system using liquid oxygen and liquid hydrogen. It incorporates forced convection cooling with liquid hydrogen which after absorbing the heat flux from the chamber is

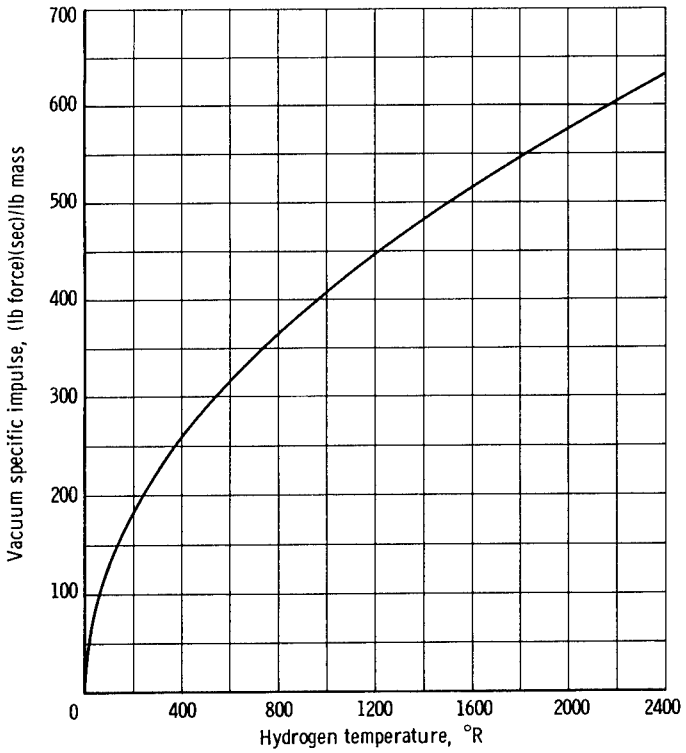

Figure 1. - Theoretical vacuum specific impulse of dumped hydrogen through infinite area ratio nozzle.

"dumped" overboard instead of being passed through the injector into the combustion chamber and burned. By this means, coolant jacket pressure drop is put in parallel with the injector pressure drop, and the propellant tanks can be pressurized to a lower pressure than is possible for a similar regeneratively cooled engine, which results in a potential weight saving in propellant tanks and pressurant or pumps. After the coolant passes from the cooling jacket, it is further utilized by being accelerated in a covergent-divergent nozzle as it is being dumped. In this way some of the available energy of the coolant can be reclaimed as thrust. The heated hydrogen provides very reasonable values of theoretical specific impulse and therefore detracts little if any from the overall specific impulse. The impulse theoretically available from the coolant is dependent on the temperature of the coolant before expansion as shown in figure 1. To optimize this system, the dump-cooled engine must be designed to raise the temperature of the coolant to the highest temperature consistent with materials in the engine by using the minimum coolant flow possible. This is unlike the design of a more conventional regeneratively cooled engine where the coolant flow is fixed and the pressure drop in the coolant jacket is minimized.

Discussed herein are the design of a dump-cooled engine and an experimental evaluation of its operation. The objective was to demonstrate the extent to which the theoretical advantages of the dump-cooled concept could be obtained in practice with real hardware and present state-of-the-art materials and to uncover problem areas in achieving the full potential.

A 500-pound-thrust rocket engine operating at a 100-psig chamber pressure with gaseous hydrogen and liquid oxygen as propellants and liquid hydrogen as a coolant was used. The engine was built of stainless steel and designed to operate at a propellant mixture ratio (O/F) of 5 (16.67-percent fuel in total propellant or equivalence ratio of 0.63) and at a coolant flow rate of 7 percent of the total propellant flow.

After the coolant passages were designed (the symbols and coolant passage design appear in appendices A and B, respectively), the off-design coolant performance of the

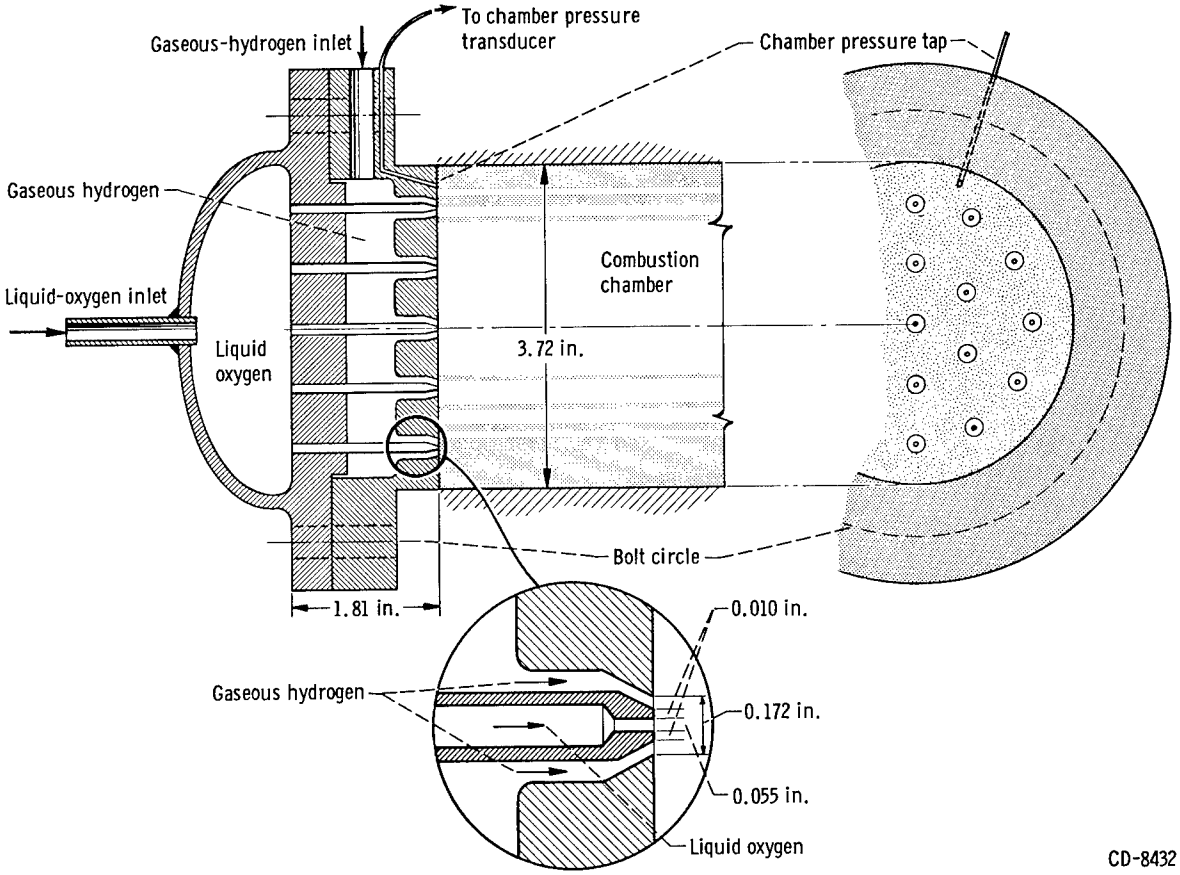

Figure 2. - Injector detail for 19-element concetric-tube injector.

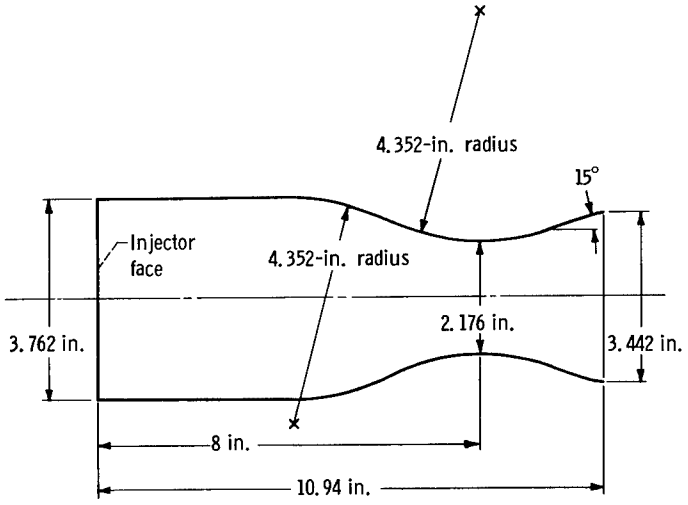

Figure 3. - Combustion chamber contour. Nominal thrust, 500 pounds; chamber pressure, 100 psig; contraction area ratio, 3; expansion area ratio, $2\frac{1}{2}$; characteristic chamber length, 20 inches.

previous design was evaluated; that is, a prediction was made of coolant temperatures and pressures in the engine for firings at O/F ratios other than 5 and coolant flows other than 7 percent of the propellant flow. This analysis is described in appendix C.

The test firings on the engine were first made at reduced propellant O/F ratios (less severe heat load) and excessive coolant flows, with subsequent firings of generally increasing propellant O/F ratio and decreasing coolant flow until the engine failed. After failure, the engine was repaired, a refractory coating (Al_2O_3) was applied to the flame-side surface, and the testing procedure was repeated. Data showing the measured and analytical heat fluxes along with coolant temperatures and pressures through the engine for various coolant flows are presented as a means of determining the minimum satisfactory coolant flow and of checking the validity of the design technique.

APPARATUS

Engine

The propellants were injected into the chamber through the 19-element concentric tube injector shown in figure 2. The liquid oxygen flowed through the center of each element while gaseous hydrogen flowed through the annulus around the oxidizer tube.

The basic combustion chamber dimensions are shown in figure 3. The contraction area ratio was 3 and with the 8-inch distance from the injector face to the throat yielded an L^* of 20 inches. When operating at a 100-psig chamber pressure, the engine produced about 500 pounds of thrust at sea level with a nozzle expansion area ratio of 2.5.

The combustion chamber, figures 4 and 5, was built of two concentric shells of 0.100-inch-thick 304 stainless steel with a 0.10-inch radial gap between the shells serving as the coolant passage. Because of the extreme difficulty of obtaining a precise dimensional gap variation between shells where the gap is varied to produce a desired optimum local coolant velocity, the gap was made constant and rather large (0.10 in.), and desired coolant velocities were achieved by means of a spiral flow path. (The helix angle was varied along the length to make the coolant velocity everywhere optimum. See appendix B for the actual helix design.) Eight helical spacers (flexible angle strips) were interposed between the two shells to direct the coolant in eight parallel spiral paths and to maintain the concentricity of the two shells. The helical spacers were attached to the outer shell and made to spring against the inner shell (see fig. 5(a)). This construction allowed the two shells to expand axially relative to one another by the inner shell sliding across the spacers. The outer shell was attached to the inner shell at the exit end by a rigid manifold and at the injector end by a flexible bellows manifold; the bellows accommodated the axial thermal expansion of one shell relative to the other. The slight radial

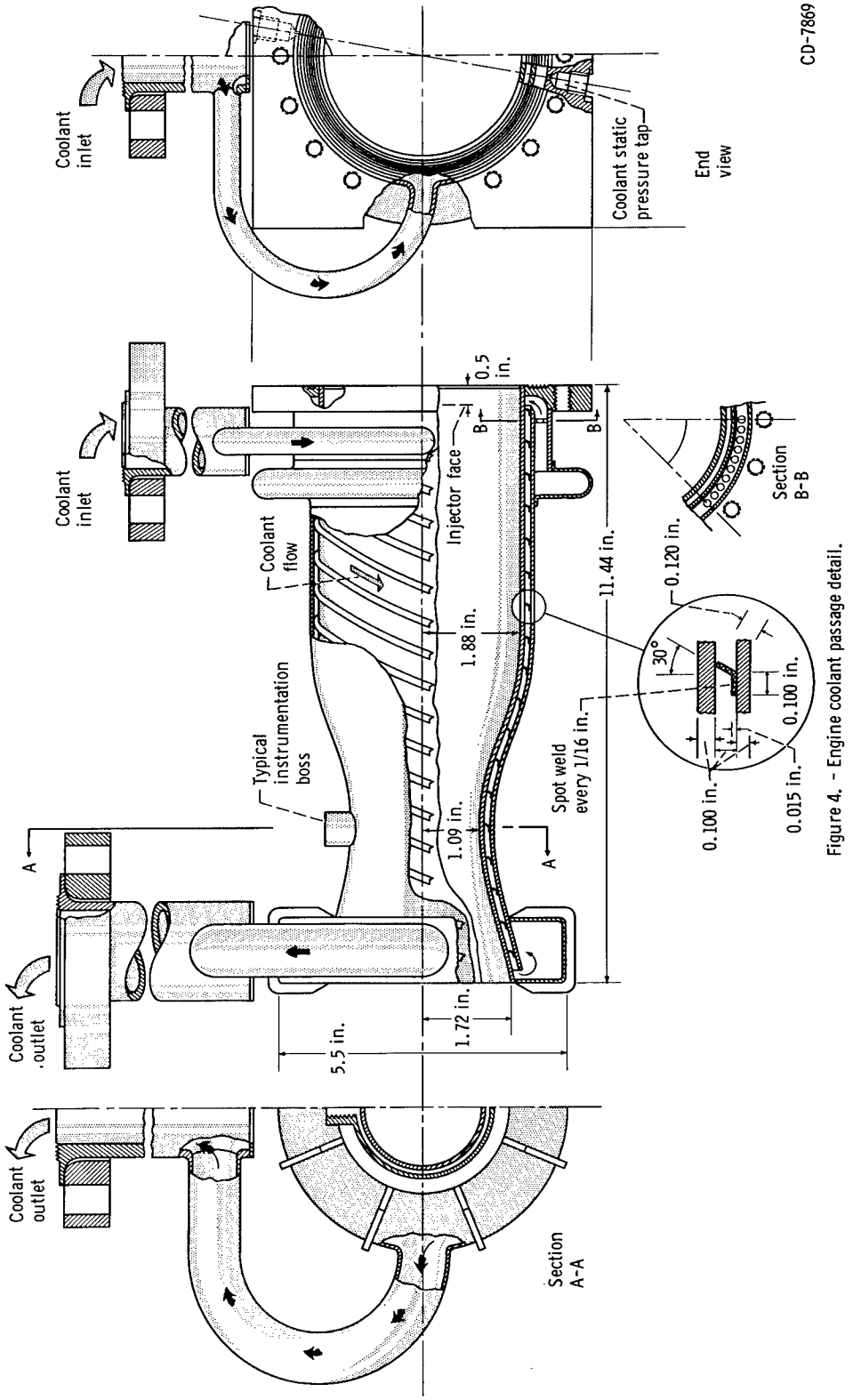

Figure 4. - Engine coolant passage detail.

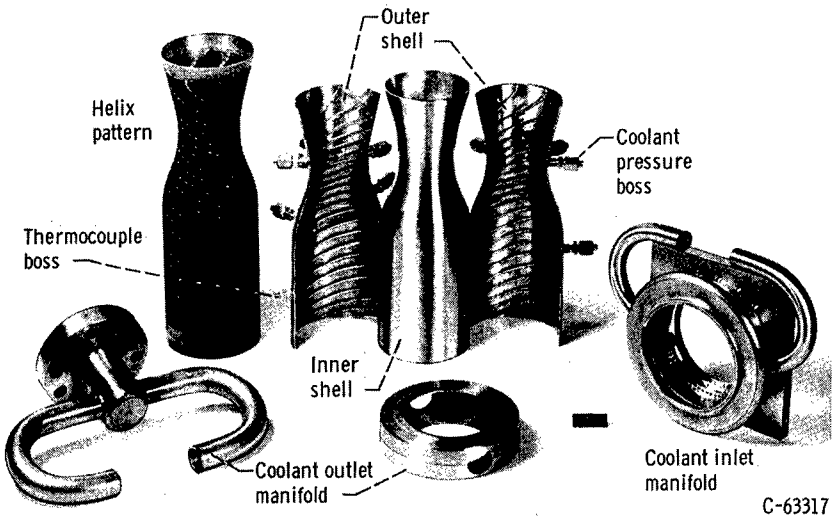

(a) Prior to final assembly.

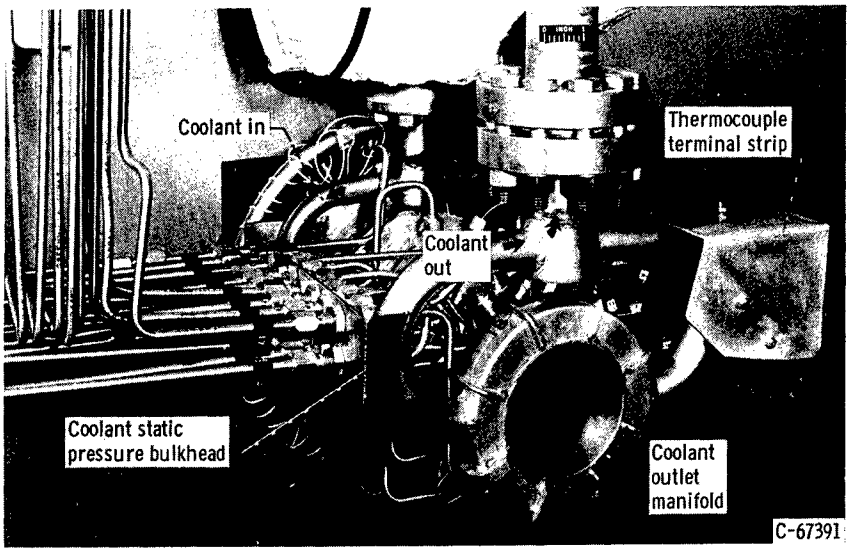

(b) Assembled and installed.

Figure 5. - Dump-cooled engine.

differential expansion of the two shells was accommodated by a slight flexing of the spacers. The assembled engine is shown in figure 5(b).

Description of Test Cell and Instrumentation

The gaseous-hydrogen propellant was supplied from a series of high-pressure-storage bottles, while the liquid oxygen was supplied from a tank immersed in liquid nitrogen. The coolant (liquid hydrogen) was stored in a vacuum-jacketed tank immersed in a liquid-nitrogen bath (see fig. 6). The coolant passed from the tank to the engine

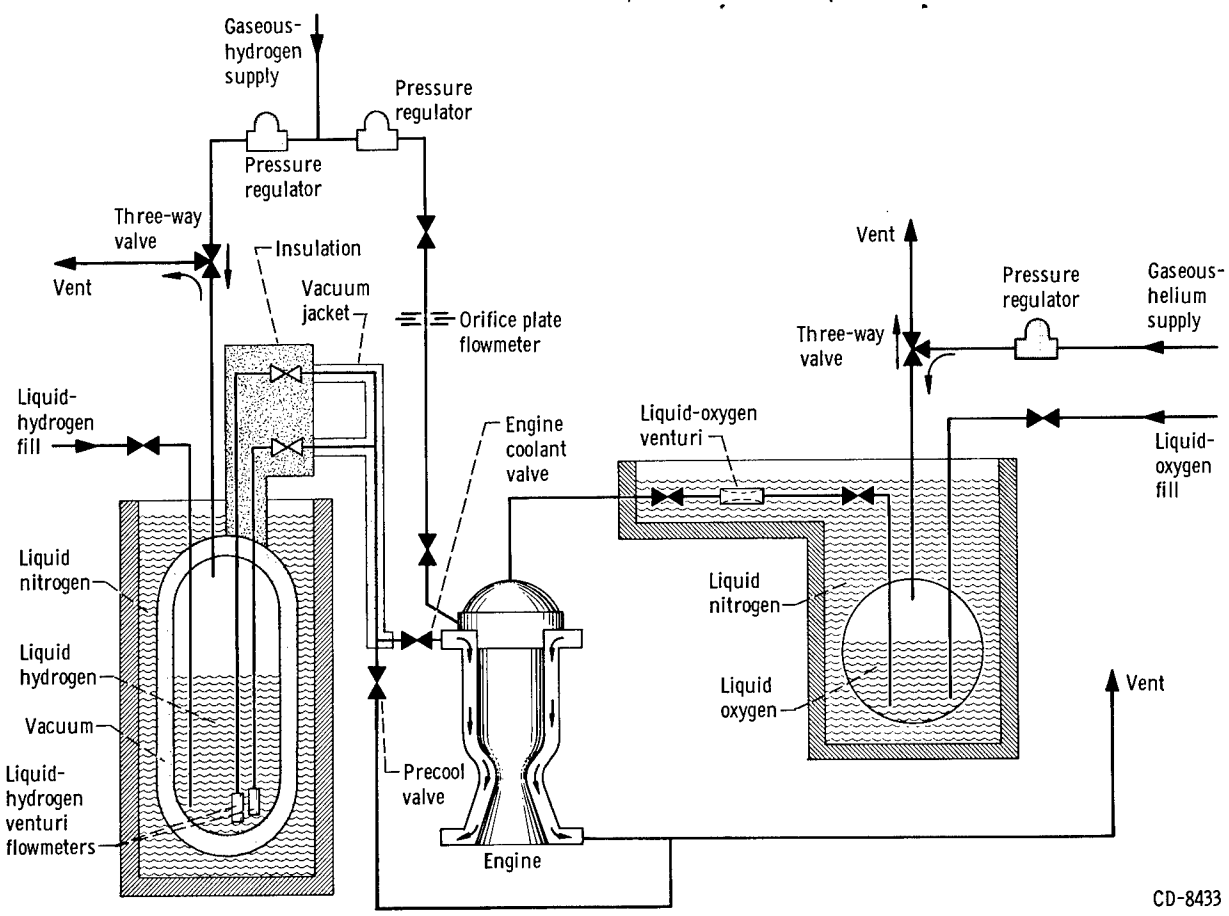

Figure 6. - Cell piping schematic.

through vacuum-jacketed piping. After the coolant passed through the engine and into the coolant exit manifold (fig. 4), its thermodynamic state was determined by measurements of temperature and pressure. Heat addition from ambient to the coolant was calculated to be negligible. The coolant was then ducted to a vent stack and released instead of being expanded through a convergent-divergent nozzle for additional engine thrust. The potential thrust of the coolant can be determined by using figure 1.

The liquid-hydrogen and liquid-oxygen flow rates were measured with venturi flowmeters while the gaseous-hydrogen flow rate was measured with a standard sharp-edge orifice. Eighteen static pressure and eighteen temperature measurement stations were located on the engine as shown in figure 7, which is a developed map of the coolant passages. All pressure measurements were taken with strain gage electrical transducers calibrated with a precision Bourdon gage accurate to within ±0.25 percent. Coolant bulk temperatures were measured with open ball thermocouples, which were made with 0.005-inch-diameter copper and constantan wires that protruded to the coolant passage midstream. The thermocouple reference junctions were placed in a calibrated thermal oven. Coolant supply temperatures in the liquid-hydrogen tank and in the supply piping

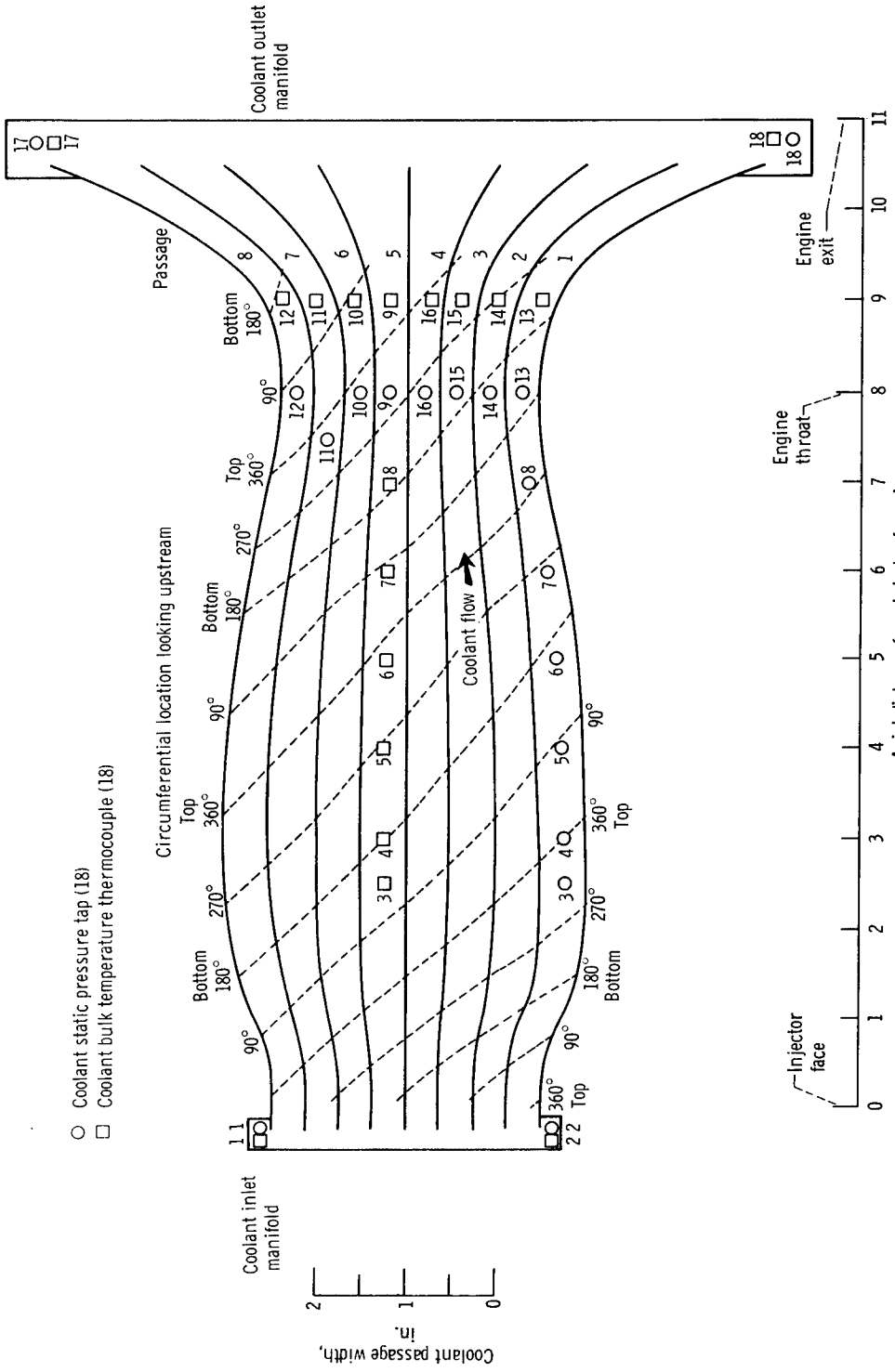

Figure 7. - Coolant passage map.

TABLE I. - FIRINGS PERFORMED ON DUMP-COOLED ROCKET ENGINE

[Chamber pressure, 100 psig.]

Firing	Mixture ratio, O/F	Coolant flow, W_c, lb/sec	Coolant, $\frac{W_c}{W_o + W_F} \times 100$, percent	Calculated combustion chamber total temperature, ^oR
Original uncoated engine				
1	2.27	0.179	11.4	3910
2	3.21	.162	9.5	4540
3	2.76	.149	9.4	4265
4	3.48	.153	8.6	4685
5	5.44	.148	8.3	5405
6	3.21	.129	7.7	4540
7	3.57	.136	7.7	4730
8	4.84	.142	7.8	5235
9	5.01	.142	7.8	5290
10	4.97	.137	7.5	5280
Repaired engine with flame-sprayed refractory coating				
11	5.01	0.174	9.7	5290
12	5.46	.133	7.5	5410
13	5.35	.125	6.9	5385
14	5.25	.120	6.9	5360

were measured with 0.1-watt carbon resistors calibrated to within an accuracy of 0.5^o R at liquid-hydrogen temperatures. Thrust was measured with a strain gage load cell and calibrated in the thrust stand with the engine in place to account for the stiffness of all the connected plumbing. The data were recorded on a high-speed digital tape for automatic computation. Some pertinent data (thrust, chamber pressure, oxidant flow, fuel flow, coolant flow, etc.) were also recorded on a multichannel oscillograph.

PROCEDURE

Firing Description

The engine was mounted in a horizontal thrust stand with insulated piping supplying the coolant. The coolant piping was cooled prior to a firing by flowing liquid hydrogen through it and through the liquid-hydrogen precool valve into the coolant vent system (see fig. 6). When the carbon resistor just upstream of the precool valve indicated liquid-hydrogen temperature, the engine firing sequence was started. The precool valve was held open until the engine coolant valve opened, at which time the precool valve closed. This technique maintained continuous flow through the piping during engine startup, which insured cold coolant delivery to the engine.

The engine was then fired for 10 seconds, which was proven by the data to be adequate for thermal equilibrium in the coolant passages. Data were obtained during the whole firing duration although heat-transfer data for only the last 3 seconds were used. As shown in table I, ten successful firings were accomplished under progressively more severe conditions before the engine failed. It failed by melting part way through the inner shell immediately upstream of the throat region. The engine was then repaired by welding the melted zone back to the original thickness. A 0.033-inch-thick coat of aluminum

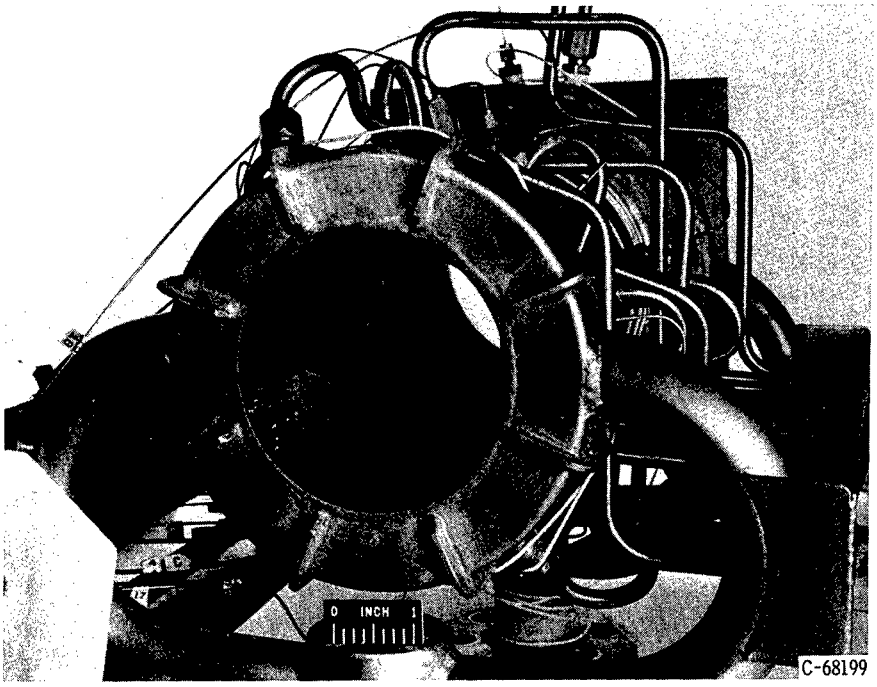

(a) After successful firing 10.

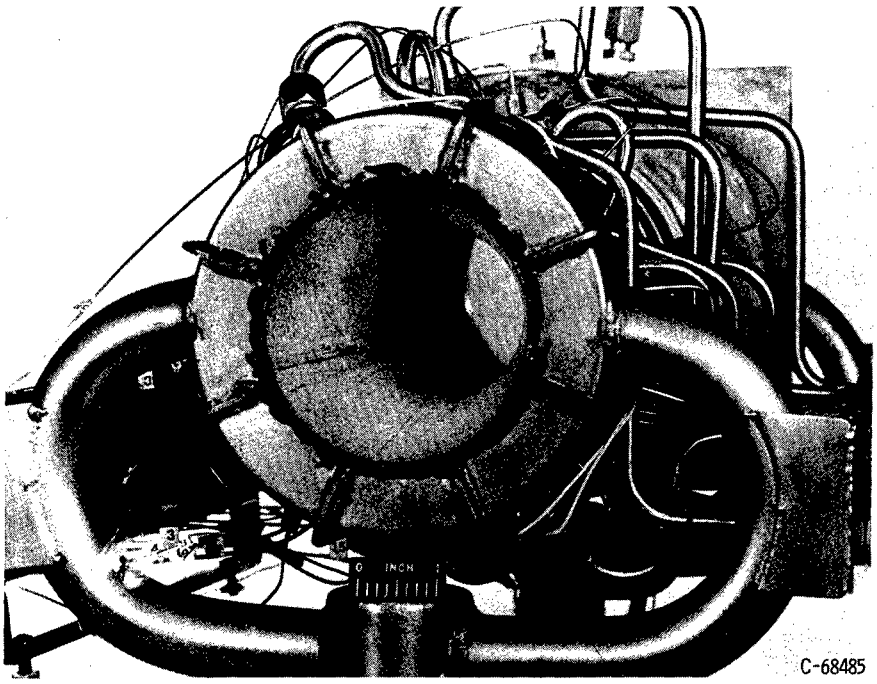

(b) After successful firing 14.

Figure 8. - Engine failure that occurred during the firing after the successful firing.

oxide was then applied to the entire flame-side surface. Another series of firings was then conducted with four successful firings accomplished before the engine again failed by melting through the repair weld.

Figure 8 shows the damage caused by the firings after the successful firings 10 and 14. The metal flowed out of cavities that formed 1/2 inch upstream of the engine throat (at $7\frac{1}{2}$ in. from injector face). The cavities formed were about half way through the metal thickness (1/4 in. wide and about 1/2 inch long).

Data Reduction

Combustion performance data were obtained on each firing by measuring chamber pressure and propellant flow rates and were checked by measuring thrust.

Heat-transfer data were reduced on a digital computer. The program inputs consisted of coolant temperatures and pressures (read from faired curves through the experimental measurements), coolant flow rate, and engine geometry parameters (including passage hydraulic radius, heat-transfer surface area, and coolant flow area, see appendix D). Since it was found that the transport properties used in appendix B were incorrect (ref. 1), improved transport properties (ref. 2) were curve-fitted for a computer subroutine. Steady-state forced-convection turbulent-flow equations (as in appendixes B and C) were used to determine heat-transfer coefficients for the flame side of the test engine with and without the refractory coating. The engine was divided axially into 44 imaginary 1/4-inch increments from which the experimental heat flux was calculated.

Since the coolant bulk temperature, pressure, and flow rate were known, the experimental heat flux was calculated by

$$q_{exp} = W_c \frac{C_{p,c,b}(T_{c,b,x} - T_{c,b,in})}{A_{sur}} \tag{1}$$

It follows from steady-state one-dimensional heat transfer that

$$T_{w,c} = \frac{q_{exp}}{h_f} + T_{c,b} \tag{2}$$

and (see fig. 9(a))

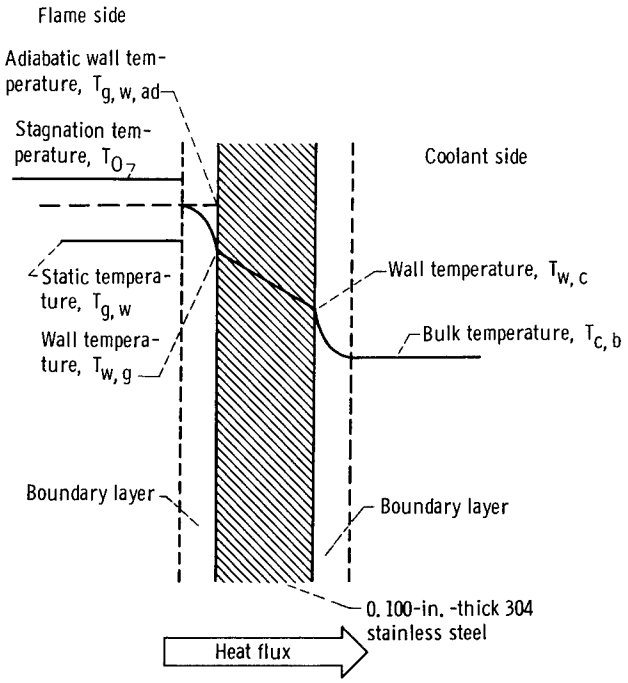

(a) Model gradient.

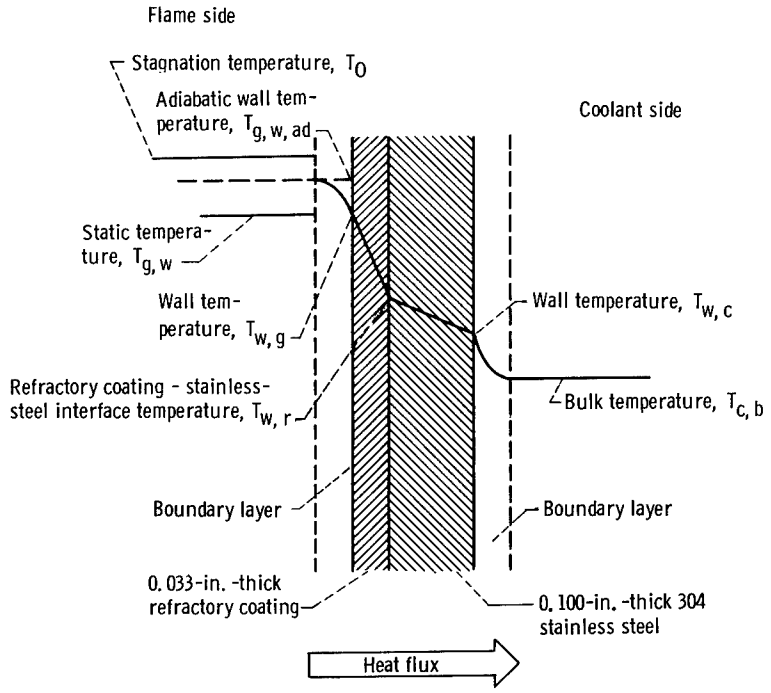

(b) Gradient for engine with refractory coating.

Figure 9. - Temperature gradient.

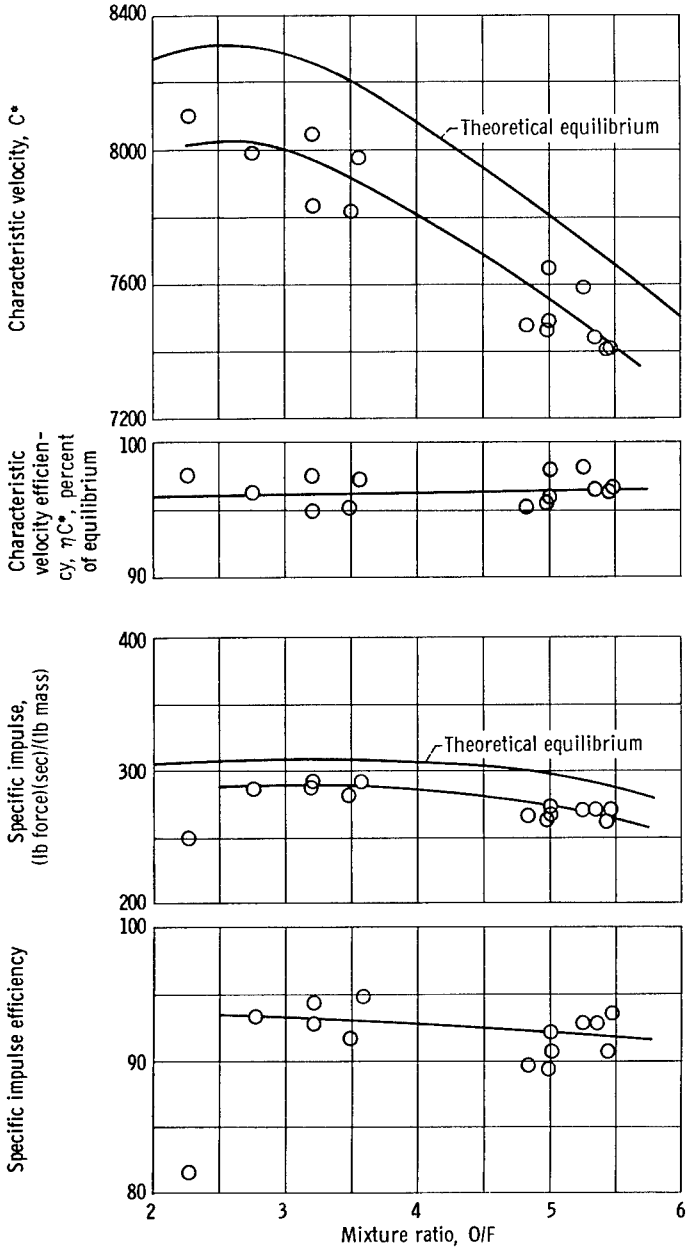

Figure 10. - Engine combustion performance. Propellants, liquid oxygen and gaseous hydrogen; chamber pressure measured at injector face, 100 psig.

$$T_{w,g} = T_{w,c} + \frac{q_{exp}\, t_w}{k_w} \tag{3}$$

For the engine with the refractory coating, the refractory interface resistance was neglected. Subsequently (see fig. 9(b)),

$$T_{w,g} = T_{w,r} + \frac{q_{exp}\, t_r}{k_r} \tag{4}$$

RESULT AND DISCUSSION

Engine combustion performance in terms of characteristic velocity and characteristic velocity efficiency is presented in figure 10(a). Experimental characteristic velocity was calculated by the use of measured nozzle throat area and measured injector-face chamber pressure and propellant flow rate; corrections were not made for momentum pressure loss, which was estimated to be about 2 percent.

Engine combustion performance was checked by use of measured thrust together with measured propellant flow rate. Specific impulse and specific impulse efficiency are presented in figure 10(b). The ratio of specific impulse efficiency to an assumed thrust coefficient efficiency of 0.983 provided a characteristic velocity efficiency that agrees within ±1 percent with the characteristic velocity efficiency of figure 10(a) if the latter is corrected for an estimated 2 percent momentum pressure loss.

Discussion of Original Configuration (First 10 Firings)

Coolant pressures and temperatures that were measured for a typical firing are shown in figures 11(a) and (b). (Pressures and temperatures for all the firings are tabulated in appendix E.) Faired curves through the data, like those of figure 11, were then used as program inputs to calculate the heat fluxes reported later. Also shown on figure 11 are analytical curves from the performance prediction described in appendix C.

Figure 11(a) presents a plot of coolant static pressure along the length of the engine in one coolant passage (passage 1). The circumferential plot shows the coolant static pressure distribution at the throat location of the engine. The axial instrumentation in coolant passage 1 was assumed to be representative of all the passages. In general, the coolant static pressure data for all firings followed the analytical curves: in the case of firings at O/F = 3, less than 7 percent above analytical, and for firings at O/F = 5,

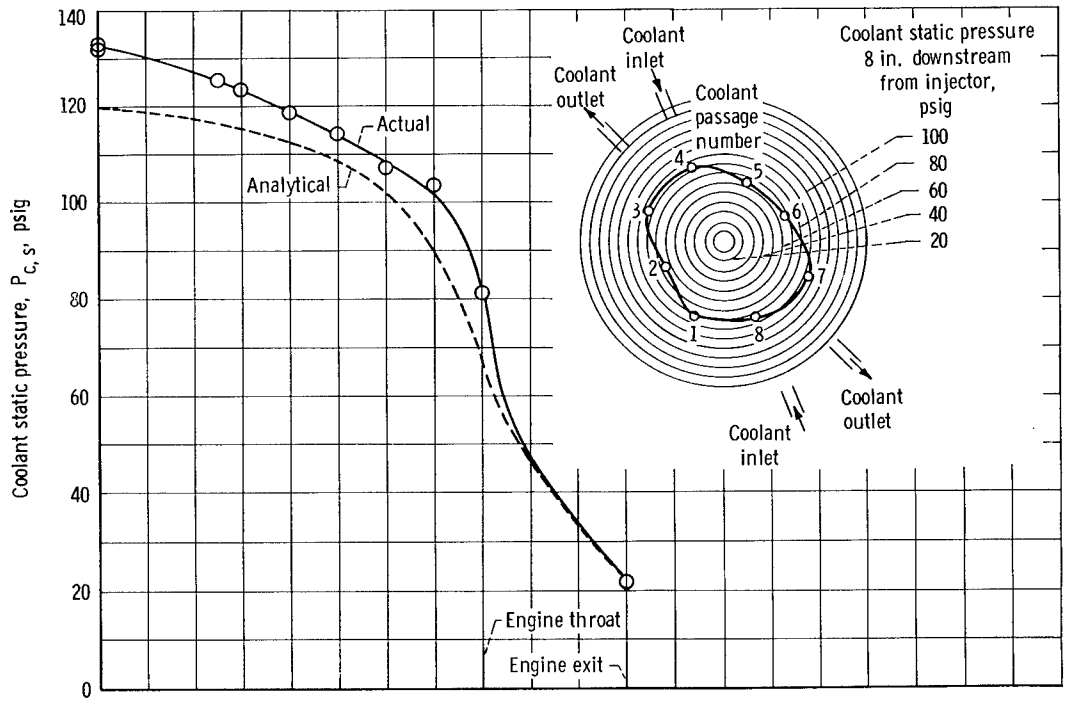

(a) Coolant static pressure in passage 1 and throat distribution for all passages.

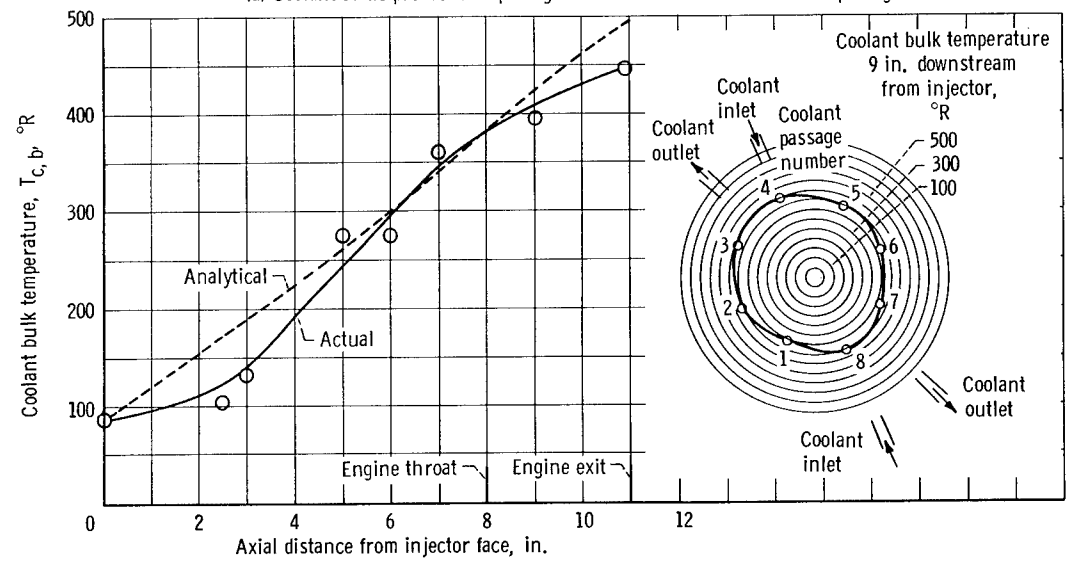

(b) Coolant bulk temperature in passage 5 and distribution for all passages at 9 inches.

Figure 11. - Typical coolant measurements in coolant passage. Firing 2; chamber pressure, 100 psig; mixture ratio, 3.21; coolant flow, 0.162 pound per second.

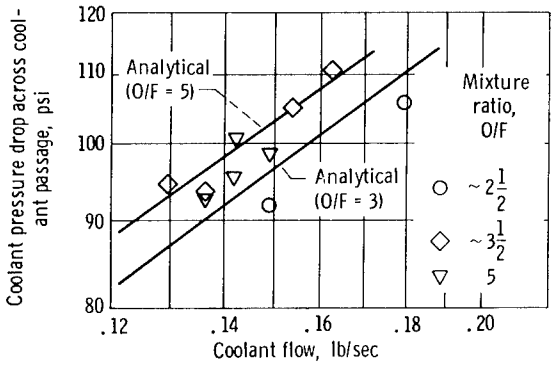

Figure 12. - Effect of coolant flow on pressure drop across coolant passage.

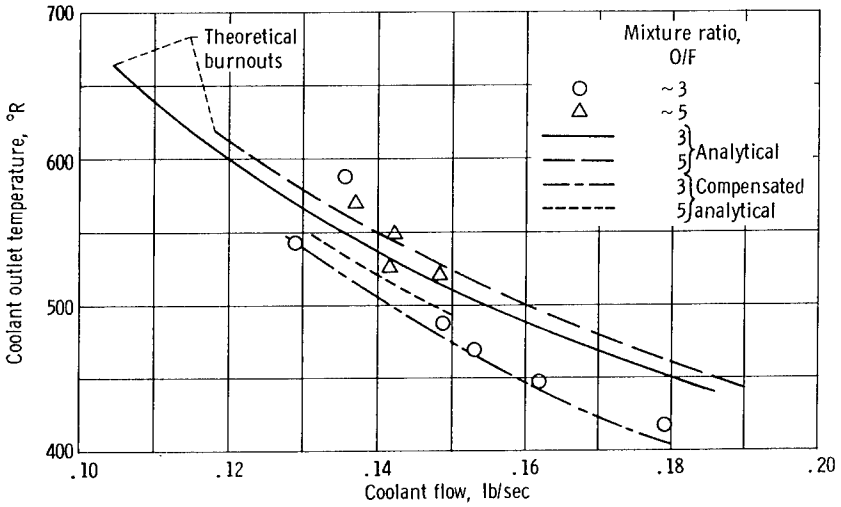

Figure 13. - Effect of coolant flow on coolant outlet temperature at several mixture ratios.

less than 3 percent below analytical. The variation between experiment and analysis is apparently analysis error caused by the simplified friction factor used in appendix B (eq. (B20)).

Figure 11(b) presents a plot of coolant bulk temperature along the length of the engine in one coolant passage (passage 5). The circumferential plot shows the coolant bulk temperature distribution at an axial location of 1-inch downstream of the engine throat. The circumferential unbalance is small enough to assume that the axial instrumentation is representative of all the passages. A pertinent point of figure 11(b) is that the experimental axial coolant bulk temperature distribution varies from the analytical significantly and similarly for all firings. Over the first 2 inches, the slope was much less than analytical, which indicated a much lower heat flux in this region than analytical. The analysis assumed that all of the combustion occurred in zero length at the beginning of the combustion chamber. It was known that the combustion would take a finite length to become complete; however, the exact length was not known so the conservative assumption was made (zero length). This assumption appeared to cause the discrepancy in the first 2 inches. In the region from 3 to 7 inches on figure 11(b), the actual data had a greater slope than the analytical. Therefore, the actual heat flux in this region was greater than predicted; this was true to slightly varying degrees for all firings.

The coolant pressure drop through the coolant jacket (while the engine is firing) is given as a function of coolant flow in figure 12. Analytical lines for O/F ratios of 3 and 5 are included as are the data points from the first 10 firings, coded to show approximate O/F ratios. As with figure 11(a), the coolant static pressure drop through the engine for firings of $O/F = 3$ was slightly above analytical predictions and for $O/F = 5$ slightly below analytical.

Coolant outlet temperature as a function of coolant weight flow for the first 10 firings, coded as to O/F ratio of the firings, is shown in figure 13. Also included are analytical curves for O/F ratios of 3 and 5 and analytical curves that were compensated for the depressed heat flux phenomena in the first 3 inches of the engine. (The exact method of compensation will be shown later.) The test data seemed to agree with the compensated analytical curves, particularly for firings at $O/F = 3$.

Heat-flux data for all of the first 10 firings are presented in figure 14, which includes a series of plots of heat flux as a function of length along the engine. Also given are analytical values for heat flux obtained from the coolant performance predictions in appendix B. The experimental heat flux was calculated every 1/4 inch from faired curves (i.e., fig. 11) through the experimental data for coolant pressure and temperature. The depressed heat-flux zone in the first few inches of engine length is clearly visible in each of these plots.

The "compensated analytical" values of figure 13 and of subsequent figures were obtained from the heat-flux plots of figure 14 in the following manner. In each case a heat-

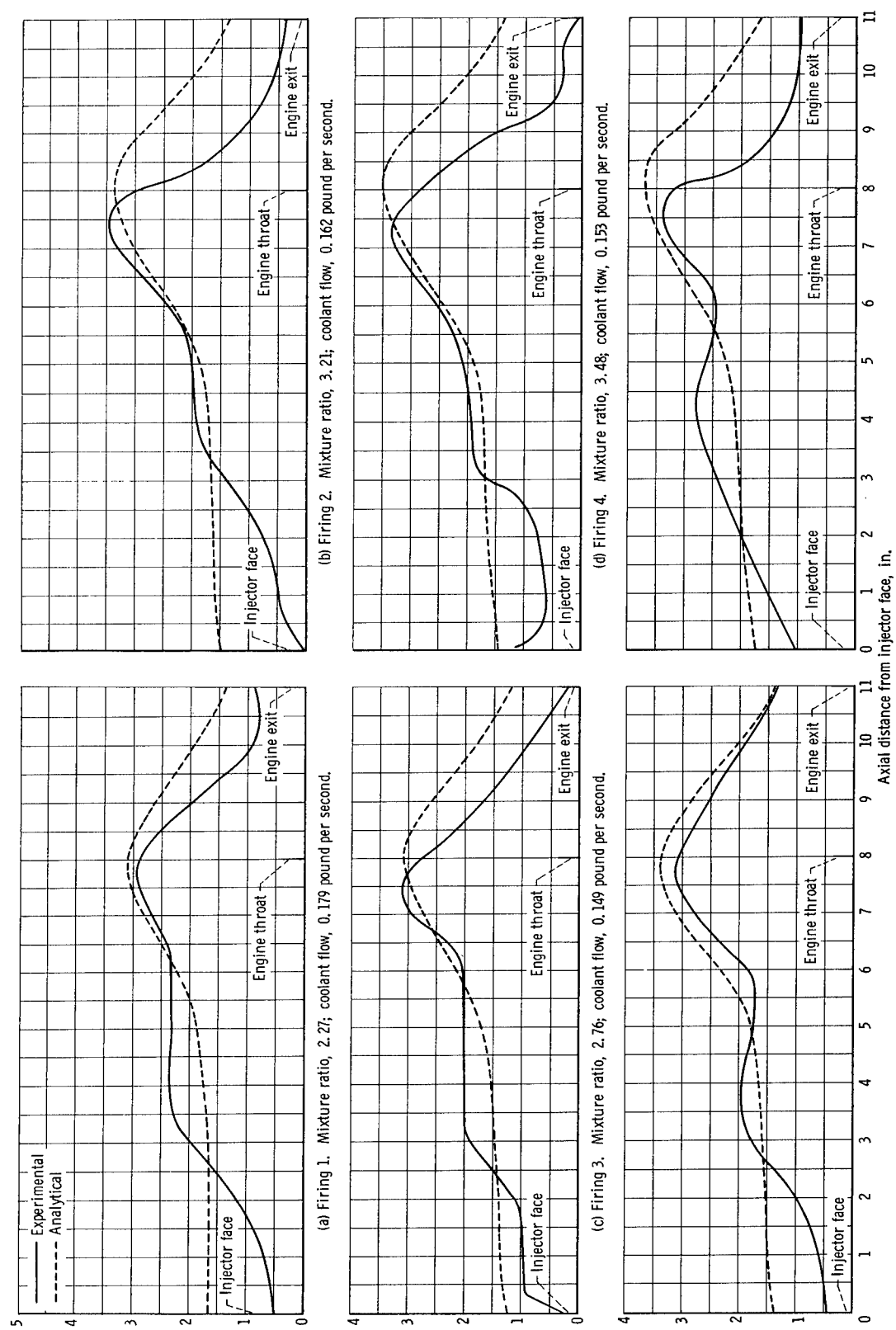

(a) Firing 1. Mixture ratio, 2.27; coolant flow, 0.179 pound per second.

(b) Firing 2. Mixture ratio, 3.21; coolant flow, 0.162 pound per second.

(c) Firing 3. Mixture ratio, 2.76; coolant flow, 0.149 pound per second.

(d) Firing 4. Mixture ratio, 3.48; coolant flow, 0.153 pound per second.

(e) Firing 5. Mixture ratio, 5.44; coolant flow, 0.148 pound per second.

(f) Firing 6. Mixture ratio, 3.21; coolant flow, 0.129 pound per second.

Figure 14. - Heat flux distribution along length of engine. Chamber pressure, 100 psig.

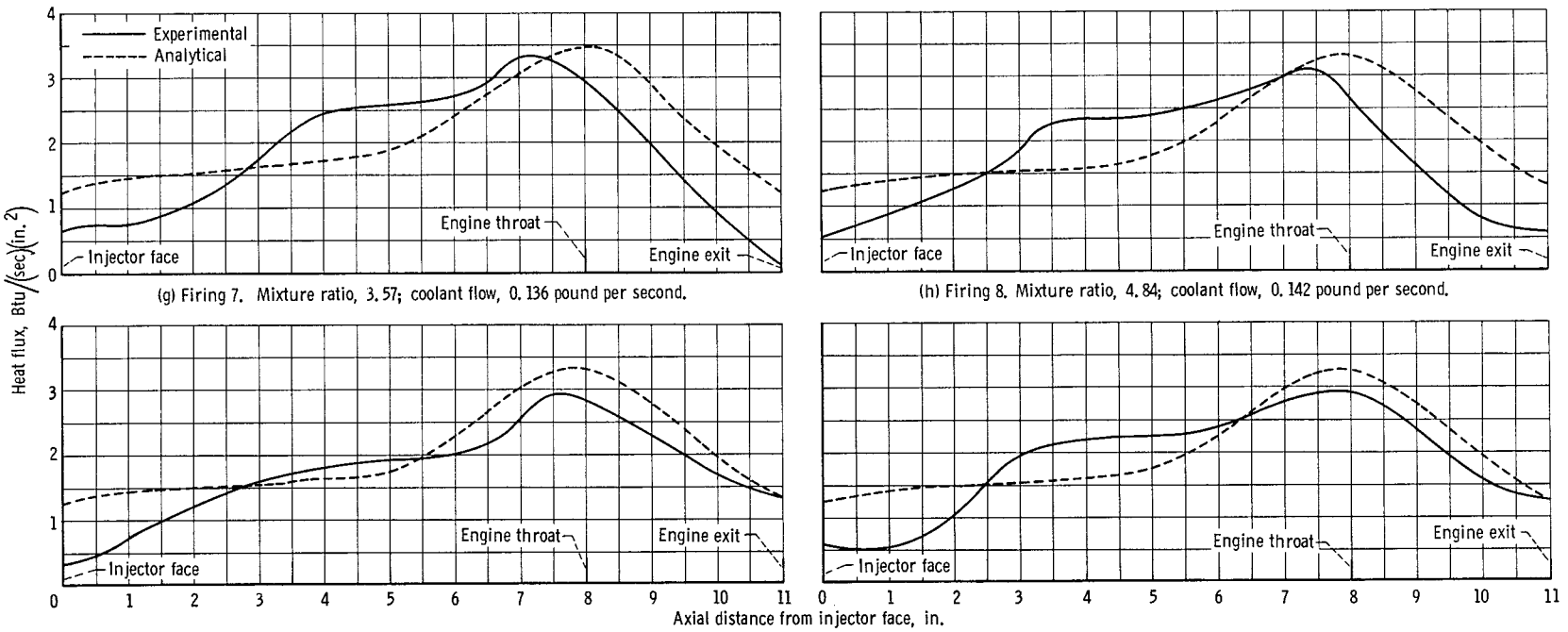

(g) Firing 7. Mixture ratio, 3.57; coolant flow, 0.136 pound per second.

(h) Firing 8. Mixture ratio, 4.84; coolant flow, 0.142 pound per second.

(i) Firing 9. Mixture ratio, 5.01; coolant flow, 0.142 pound per second.

(j) Firing 10. Mixture ratio, 4.97; coolant flow, 0.137 pound per second.

Figure 14. - Concluded.

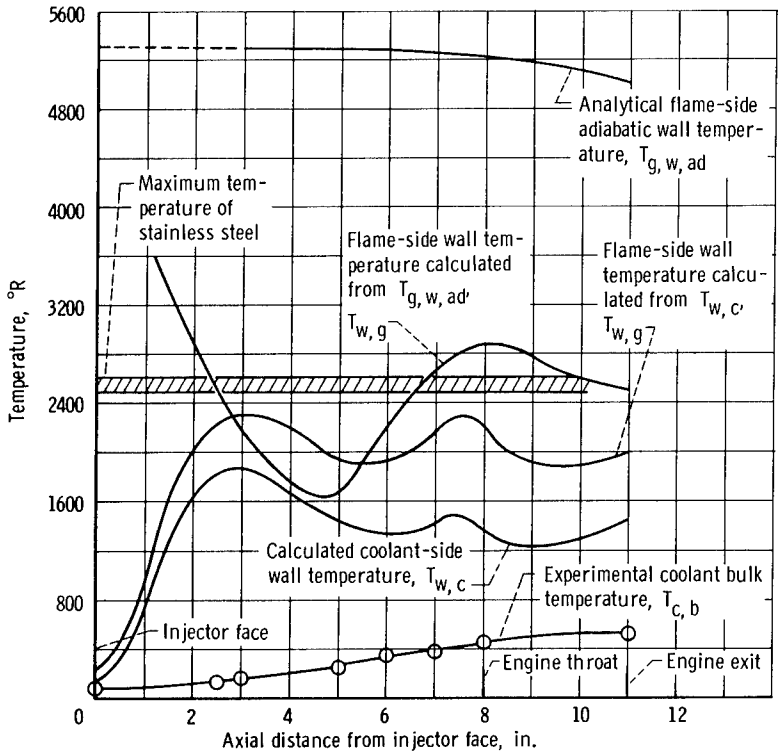

Figure 15. - Typical temperature distributions through engine. Firing 9; chamber pressure, 100 psig; mixture ratio, 5.01; coolant flow, 0.142 pound per second.

flux distribution was assumed that was identical to the experimental for the first 3 inches and identical to the analytical for the remaining 8 inches of engine length. From this assumed heat flux and measured coolant flow rates, the coolant outlet temperatures and pressures were calculated by using the analytical values for heat-transfer coefficients (as in appendixes A and B). These results were then plotted as "compensated analytical." Instead of comparing experimental to analytical data, a comparison can be made to compensated analytical and thereby eliminate the depressed heat-flux effects of the first 3 inches of the engine.

Other consistent tendencies in the data can be noted from figure 14. In the region from 3 to 7 inches from the injector face, the heat flux was generally higher for all firings than the analysis predicted. In the region from 8 to 11 inches from the injector face, the heat flux was consistently lower than predicted by analysis. The magnitudes of these phenomena are nearly the same, so that the net effect on total heat load to the coolant is approximately zero.

Temperature distributions through the engine for a typical firing are presented in figure 15. The heat flux for this firing is shown in figure 14(i) (firing 9). The bottom curve of figure 15 is the experimental coolant bulk temperature $T_{c, b}$ that was measured during the firing (i. e., see fig. 11(b)). From this faired curve were calculated

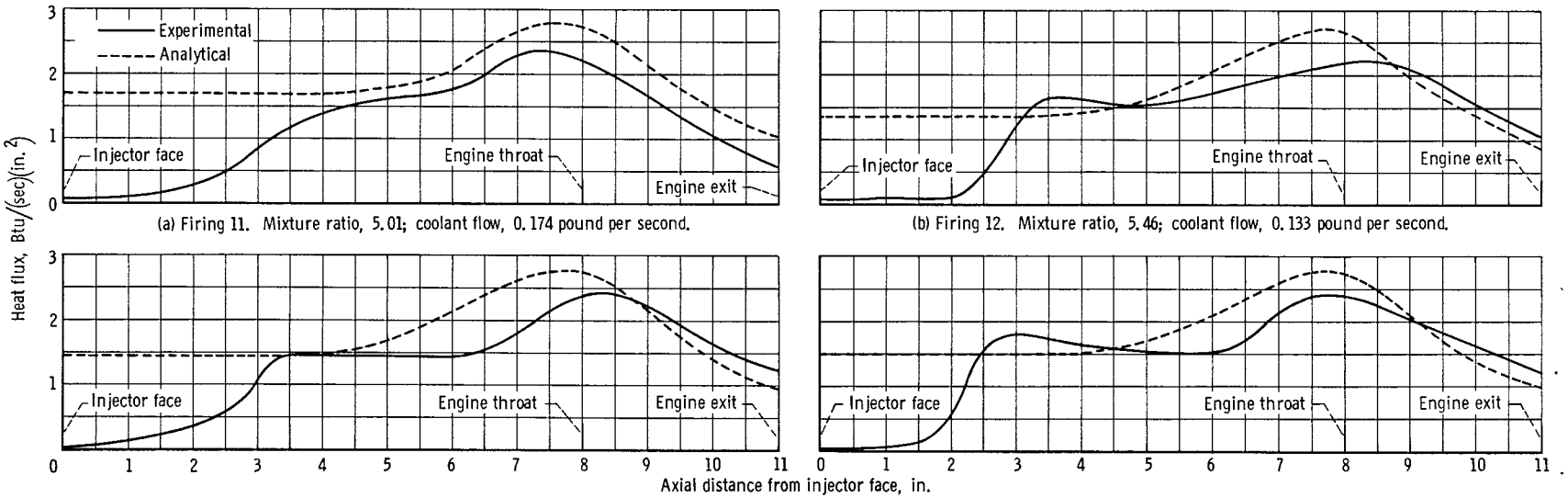

(a) Firing 11. Mixture ratio, 5.01; coolant flow, 0.174 pound per second.

(b) Firing 12. Mixture ratio, 5.46; coolant flow, 0.133 pound per second.

(c) Firing 13. Mixture ratio, 5.35; coolant flow, 0.125 pound per second.

(d) Firing 14. Mixture ratio, 5.25; coolant flow, 0.120 pound per second.

Figure 16. - Heat flux distribution along length of engine with refractory coating. Chamber pressure, 100 psig.

the experimental heat flux q_{exp}, the analytical coolant-side-heat transfer coefficient h_c, the coolant-side metal temperature $T_{w,c}$, and the flame-side metal temperature $T_{w,g}$. The top curve on the figure is a plot of analytical flame-side adiabatic wall temperature $T_{g,w,ad}$; from it, together with the experimental heat flux and analytical flame-side heat-transfer coefficients, another flame-side wall temperature was calculated and plotted. A comparison of the two flame-side wall temperatures shows fair agreement, with one less than 440° R below the other in the region from 3 to $5\frac{1}{2}$ inches from the injector face, and less than 680° R above the other in the region from $5\frac{1}{2}$ to 8 inches. Because of the significant possible error inherent in the use of the analytical adiabatic wall temperature ($T_{g,w,ad}$), the flame-side wall temperature calculated from the coolant is considered more correct than the flame-side wall temperature calculated from the analytical adiabatic wall temperature. The difference in these flame-side wall temperatures again points out the difference in heat load distribution between experimental and analytical as noted in figure 14.

As is shown in figure 15, it appears that the design reasonably optimized coolant velocity over the main portion of the chamber by holding metal temperature nearly constant ($T_{w,g}$ calculated from $T_{w,c}$ in fig. 15) and equal to the material limit except for two zones of over-cooling. These zones were in the first 3 inches of chamber length and the zone downstream of the engine throat. Further gains in cooling performance in terms of lower coolant flow and higher coolant exit temperatures would be possible by careful redesign.

Discussion of Firings on Refractory Coated Engine

A refractory coating is often applied to the flame-side surface of rocket engines to insulate the metal from the hot combustion gases and to facilitate cooling. This coating results in a lower heat load to the coolant, with a lower pressure drop through the coolant jacket, and/or a lower coolant outlet temperature. The effect such a refractory coating (0.033-in.-thick aluminum oxide) had on a dump-cooled configuration was investigated in firing 11 through 14. Heat-flux data for these firings are shown in figure 16, which is a series of plots of heat flux as a function of length along the engine. Shown also are analytical curves obtained from the coolant performance prediction in appendix C. The experimental and analytical heat-flux data agree very well, except near the injector, with the experimental generally somewhat lower than the analytical.

Typical temperature distributions through the engine are shown in figure 17 (firing 11). Two calculated flame-side wall temperatures are again shown; one was calculated from the analytical adiabatic wall temperatures, and the other from the flame-side metal temperatures, as were the similar curves of figure 15. The comparison between the ana-

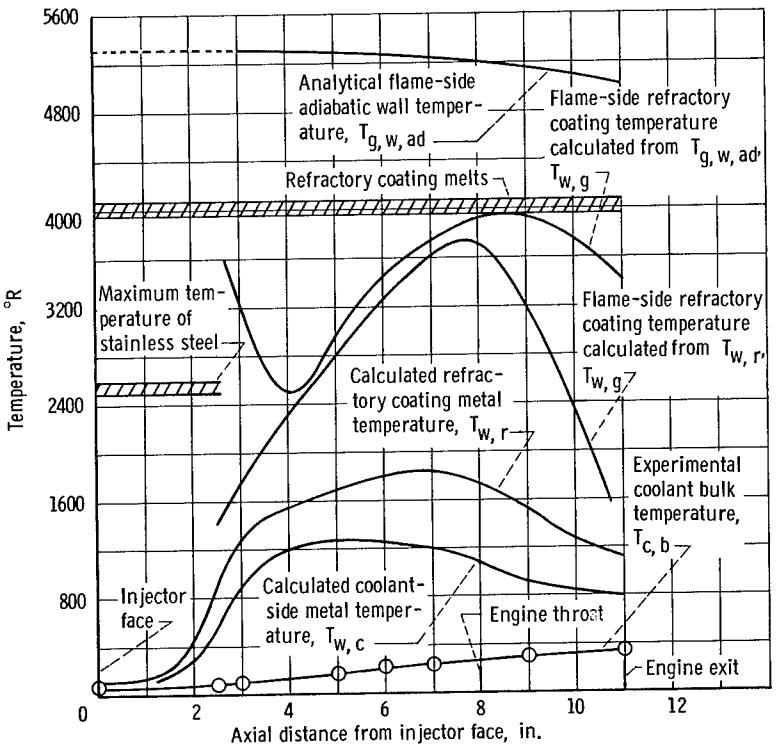

Figure 17. - Typical temperature distributions through engine with refractory coating. Firing 11; chamber pressure, 100 psig; mixture ratio, 5.01; coolant flow, 0.174 pound per second.

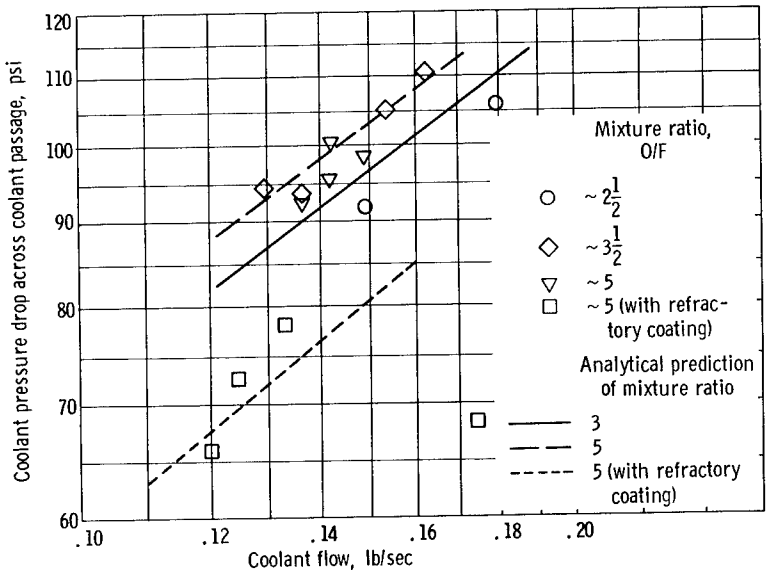

Figure 18. - Effect of coolant flow on pressure drop across coolant passage. (Refractory coated engine data included.)

lytical and experimental heat fluxes of figure 16 is similar to the comparison of the two calculated flame-side wall temperatures of figure 17. The flame-side wall temperature at the throat of the engine is shown as very near the melting point of the refractory coating, which also agrees with the fact that a very slight glazing and flowing of the coating was observed at the throat of the engine after the firing was completed. Similar glazing was observed after firing 14 and is shown in figure 8(b).

Figure 18, which presents a plot of coolant pressure drop across the engine as a function of coolant flow, is a repeat of figure 12 with the refractory coating engine data added. Shown are the data points from the last four firings along with the analytical prediction for these points. The effect that the refractory coating had on coolant pressure drop is clearly shown in this figure; at a given coolant flow, the pressure drop was decreased approximately 20 to 30 psi.

Coolant outlet temperature as a function of coolant flow is shown in figure 19, which is a repeat of figure 13 with the refractory coating engine data added. Data points from the last four firings along with the compensated analytical prediction for these points are shown. The experimental points agree well with the compensated analytical curve (compensated for the depressed heat flux zone in the first 3 in. of chamber length). At the same coolant flow (and combustion conditions), coolant outlet temperature was decreased by approximately 90° to 100° R by the addition of the refractory coating.

The minimum satisfactory coolant flow for the coolant design of this engine with and

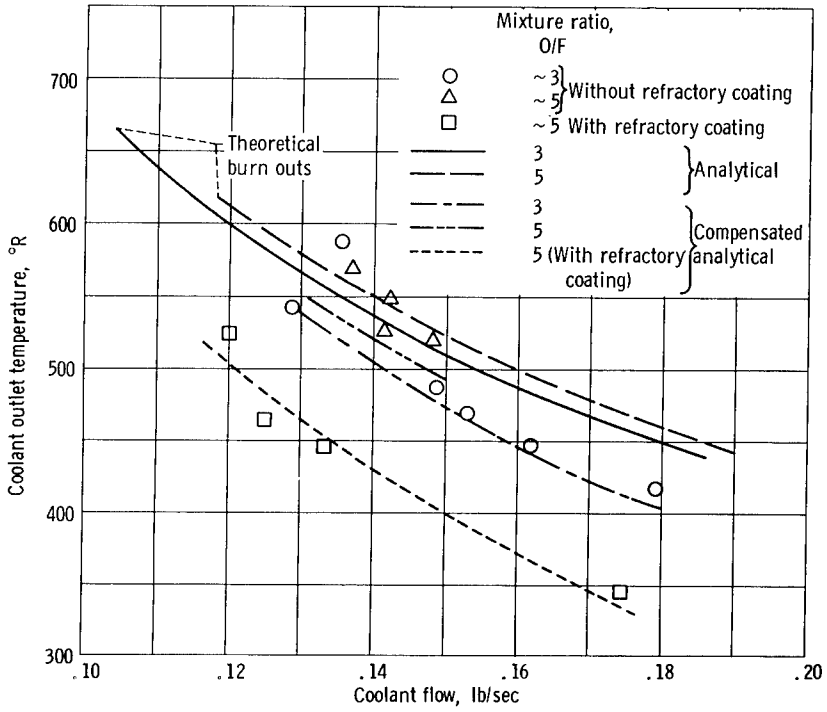

Figure 19. - Effect of coolant flow on coolant outlet temperature at several mixture ratios. (Refractory coated engine data included.)

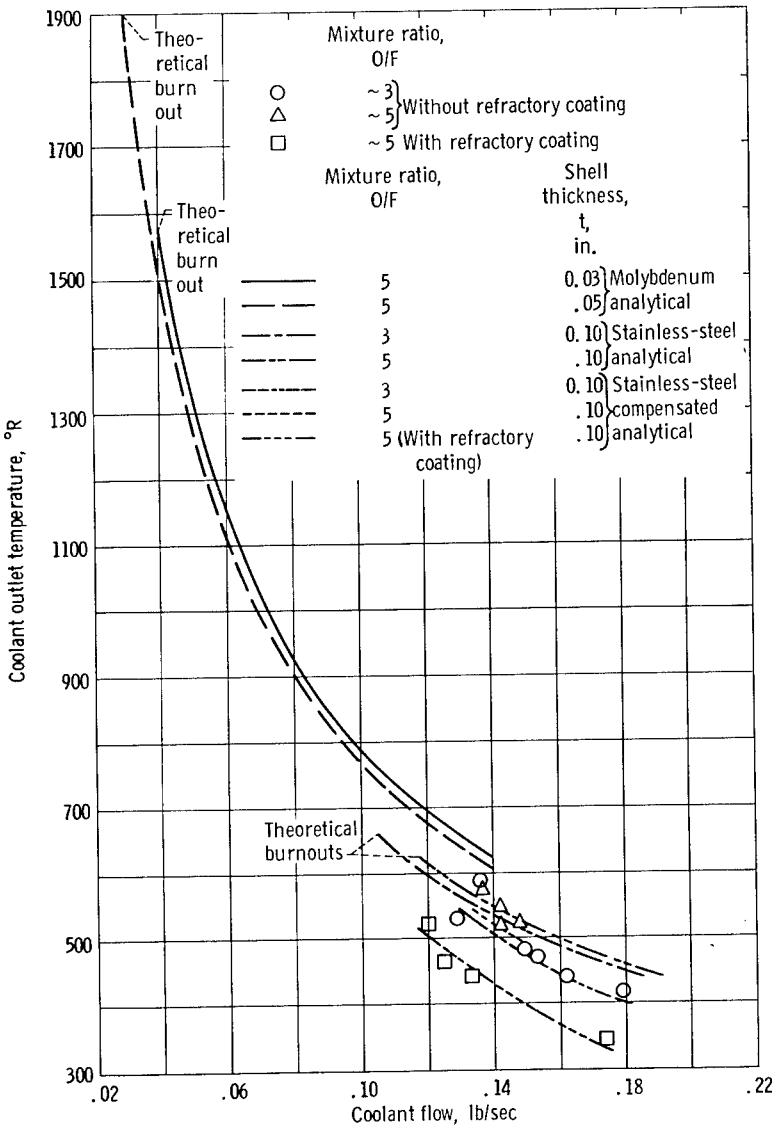

Figure 20. - Projected coolant performance of dump-cooled engine.

without the refractory coating can be assumed to be the flow reported in firings 14 and 10 (0. 120 and 0. 137 lb/sec, respectively), since these were the lowest flows successfully used. These flows are not the lowest possible for dump-cooled engines of this size, for it is believed that a careful redesign of the coolant passages of this engine using this design technique (appendices B and C and the data reported herein) would result in an engine that could operate at a lower coolant flow exiting at a higher outlet temperature.

Discussion on Projected Potential of Dump-Cooled Engines

To indicate the projected potential of an advanced design dump-cooled configuration,

a performance prediction was made (similar to appendix B) on the present coolant flow area distribution, but with a molybdenum inner shell assumed instead of the 304 stainless steel shell. Molybdenum was selected because its characteristics would indicate capabilities of most of the refractory metal alloys since it possesses high-temperature properties representative of most of these alloys. The maximum flame-side wall temperatures allowed for two cases of wall thickness were 3560° and 3160° R.

The significant results of this analysis are shown in figure 20, which presents a plot of coolant outlet temperature as a function of coolant weight flow. Also included are the experimental data previously presented in figures 13 and 19. The change from the conventional stainless-steel inner shell to a thinner molybdenum inner shell (high temperature) clearly reflected a potential for a marked decrease in coolant weight flow and increase of predicted coolant outlet temperature. At the predicted minimum coolant flow for the two molybdenum cases considered, the coolant outlet temperatures were 1900° and 1575° R, which could yield theoretical impulses up to 560 and 510 seconds, respectively (fig. 1). A further improvement to the projected performance with the molybdenum inner shell would include the design of a new coolant flow area distribution (spacer helix pattern) specifically for the molybdenum shell instead of using the existing design that was made for the stainless-steel inner shell. Though this analysis shows only the theoretical potential, it is felt that a significant amount of this potential is obtainable. By use of a refractory metal (like molybdenum), a dump-cooled engine could be designed to yield coolant specific impulses up to and perhaps even greater than the specific impulse of the main combustion process and hence provide the following two advantages:

(1) Lower propellant supply pressures, since the coolant jacket is in parallel with the injector instead of in series, which would allow for lighter tanks, less pressurant, or smaller propellant punps, etc.

(2) The energy absorbed in cooling the combustion chamber walls can be reclaimed as thrust.

CONCLUDING REMARKS

A dump-cooled engine was designed and experimentally evaluated. A 500-pound-thrust rocket engine with an expansion area ratio of $2\frac{1}{2}$ and operating at 100 psig chamber pressure with gaseous hydrogen and liquid oxygen as propellants and liquid hydrogen as a coolant was used for this investigation. It was designed to operate at a propellant O/F ratio of 5 and a coolant flow rate of 7 percent of the total propellant flow. The test firings on the engine were first at reduced propellant O/F ratios and excessive coolant flows, with subsequent firings of increasing propellant O/F ratio and decreasing coolant flow until the engine failed. At this time the engine was repaired and a refractory coating was

applied to the flame-side surface. The engine was then fired another four times before it failed again.

The design reasonably optimized coolant velocity over the main portion of the chamber, holding metal temperature nearly constant and equal to the material limit except for two zones of over-cooling. One of these zones was in the first 3 inches of chamber length and attributable to the real effects of the injector. The other zone was just downstream of the engine throat.

The minimum satisfactory coolant flow for this engine was 7.5 percent of total propellant flow and 6.9 percent for the engine with the refractory coating. This does not mean that these flows are the lowest possible for a dump-cooled engine of this size, for it is apparent that a careful redesign of the coolant passages of this engine in light of the data obtained herein, using the described design technique, would result in an engine that could operate at a lower coolant flow, which would exit at a higher outlet temperature.

The projected potential of dump-cooled engines was investigated by an analytical performance prediction that assumed a molybdenum inner shell was used with the existing coolant passage configuration. The analytical results indicated that the coolant flow could be appreciably reduced and coolant exit temperature could be made high enough to yield coolant specific impulses up to and perhaps greater than the specific impulse of the main combustion process.

Lewis Research Center,
National Aeronautics and Space Administration,
Cleveland, Ohio, March 10, 1966,
730-100-31-06-22.

APPENDIX A

SYMBOLS

A	area, $in.^2$
A_c	coolant flow area of one passage, $in.^2$
$A_{i,cs}$	inside cross-sectional area, $in.^2$ (flow area of combustion gases)
A_{sur}	surface area of inner shell, $in.^2$ (heat-transfer area)
a	spacer thickness (see fig. 21), in.
B	constant
b	spacer width, (see fig. 21), in.
C_p	specific heat at constant pressure, $Btu/(^oR)(lb\ mass)$
$C_{p,c,b}$	specific heat at constant pressure of coolant at bulk temperature
$C_{p,f}$	specific heat at constant pressure of boundary layer film
C^*	characteristic velocity, ft/sec
c	circumference, in.
D_e	equivalent diameter of coolant passage (see eq. (B11)), in.
D_i	inside diameter of inner shell, in.
d	spacer slant height (see fig. 21), in.
f	flow friction factor (coolant), dimensionless
g	gravitational conversion factor, 386.4 $(lb\ mass)(in.)/(lb\ force)(sec^2)$
h	heat-transfer coefficient, $Btu/(sec)(in.^2)(^oR)$
h_c	coolant-side heat-transfer coefficient, $Btu/(sec)(in.^2)(^oR)$
h_g	flame-side heat-transfer coefficient, $Btu/(sec)(in.^2)(^oR)$
k	thermal conductivity, $Btu/(sec)(in.)(^oR)$
k_r	thermal conductivity refractory, $Btu/(sec)(in.)(^oR)$
k_w	thermal conductivity of 304 stainless steel, $Btu/(sec)(in.)(^o R)$
L	coolant passage length, in.
L^*	characteristic chamber length, or combustion chamber volume/ engine throat area, in.
ℓ	axial length along engine from injector, in.

M	Mach number, dimensionless
m	molecular weight, lb mass/lb mole
N	number of coolant passages
Nu	Nusselt number, dimensionless
O/F	mixture ratio, W_O/W_F
P	pressure, psia
P_{in}	pressure at inlet of iterative increment, psia
P_x	pressure at outlet of iterative increment, psia
Pr	Prandtl number, dimensionless
Q	heat rate, Btu/sec
q	heat flux, Btu/(sec)(in.^{2})
R	gas constant, 10.73 (lb mass)(ft^3)/(in.^{2})(lb mole)(^{o}R)
Re	Reynolds number, dimensionless
r	radius, in.
r_1	inner shell inside radius, in.
r_2	outer shell inside radius, in.
T	temperature (see fig. 9), ^{o}R
t	thickness, in.
t_r	refractory coating thickness
t_w	metal wall-thickness of 304 stainless steel
V	velocity, in./sec
W	flow, (lb mass)/(sec)
W_o	oxident flow
X	coolant passage width, in.
Y	coolant passage height, in.
Z	chord of sector formed by angle $360^o/N$ at r_2, in. (see fig. 21)
α	helix lead angle, deg
γ	ratio of specific heats, dimensionless
δ	adiabatic recovery factor, dimensionless
η	efficiency

θ	spacer slant angle, deg
μ	viscosity, (lb force)(sec)/(in.^{2})
ρ	density, (lb mass)/(in.^{3})
ρ_m	mean density (see eq. (B19))
φ	passage width angle, deg

Subscripts:

a	sector annulus area normal to engine axis
ad	adiabatic
av	average
b	stream or bulk
c	coolant
cs	cross-sectional
e	equivalent
exp	experimental
F	fuel
f	film
g	gas (flame side)
i	inside engine
in	coolant inlet (beginning of iterative increment)
m	mean (half way between wall and bulk)
O	outside, stagnation
p	propellants (total)
r	refractory
ref	reference
s	static
sur	surface
t	total
w	wall (304 stainless steel)
x	refers to position axially along engine (end of iterative increment)

Superscripts:

M	Reynolds number exponent
N	Prandtl number exponent

APPENDIX B

DESIGN OF DUMP-COOLED ENGINE COOLING PASSAGE

The design problem was to determine the coolant flow area required to yield coolant velocities just adequate to cool the inner shell to a flame-side temperature of 2000° R. The coolant properties (density, specific heat, viscosity, etc.) are constantly changing as a function of coolant temperature and pressure, which in turn are affected by previous heat addition. Because of this condition the design must be an iterative process, satisfying first the design criteria in the first increment of engine length, and then with new iterated coolant properties, satisfying the design criteria in subsequent increments.

The design hypotheses were as follows:

Propellants	gaseous hydrogen and liquid oxygen
Propellant mixture ratio	5.0
Chamber pressure, psig	100
Temperature of liquid-hydrogen coolant supply, $^{\circ}$R	57
Pressure of liquid-hydrogen coolant supply, psia	150
Coolant weight flow, percent of total propellant flow	7
Thickness of 304 stainless steel chamber wall (2000° R on flame-side surface), in.	0.100
Number of spiral coolant passages	8
Height of spiral coolant passages, in.	0.100
Width of spiral coolant passages (variable helix angle)	variable
Characteristic velocity efficiency, percent	97

The design procedure was to establish the local heat flux q as a function of the engine axial length ℓ by using the following equation:

$$q = h_g(T_{g,w,ad} - T_{w,g}) \tag{B1}$$

The flame-side heat-transfer coefficient was determined from the basic Nusselt equation of reference 3 (p. 300):

$$Nu = B\,Re^{M}Pr^{N} \tag{B2a}$$

The flame-side gas film properties are evaluated at a film temperature defined as

$$T_{f,g} = \frac{1}{2}(T_{g,w,ad} + T_{w,g}) \tag{B2b}$$

By setting the constant B in equation (B2a) equal to 0.023 and the exponents M and N equal to 0.8 and 0.4, respectively, as is current practice, equation (B2a) can then be rewritten in a more usable form as

$$Nu_f = 0.023\, Re_f^{0.8} Pr_f^{0.4} \tag{B3}$$

If equation (B3) is written in terms of the basic parameters for the dimensionless quantities, h_g is then readily determined as

$$h_g = 0.023 \frac{k_f}{D_i}\left[\frac{W_p}{A_{i,cs}}\left(\frac{D_i}{\mu_f}\right)\left(\frac{1}{g}\right)\left(\frac{T_{g,w}}{T_f}\right)\right]^{0.8}\left(\frac{g\mu_f C_{p,f}}{k_f}\right)^{0.4} \tag{B4}$$

The temperature ratio in the Reynolds number in equation (B4) was added to correct to film conditions. For this the bulk gas temperature was assumed equal to the static temperature. This assumption does not introduce appreciable error since bulk temperature is defined (ref. 3, p. 278) as the average temperature of the quantity of fluid passing a certain cross section of flow per unit of time, and is dependent not only on the temperature of the main fluid body but also on the temperature of the fluid at the surface. Data for the static temperatures were taken from reference 1.

The adiabatic wall temperature is defined as

$$T_{g,w,ad} = T_s + T_s\left(\delta \frac{\gamma - 1}{2} M^2\right) \tag{B5}$$

It can be shown by elementary algebraic manipulations that the form of equation (B5) is the same as that given in references 4 and 5. This form was preferred herein because of the availability of γ and M data in reference 1.

In turbulent flow, the value of the factor δ increases with Reynolds number to approximately 0.90 (ref. 5). Because of the range of Reynolds numbers herein, a value of 0.88 was selected.

The temperature on the coolant side of the combustion chamber wall was then calculated by

$$T_{w,c} = T_{w,g} - q\left(\frac{t_w}{k_{w,av}}\right) \tag{B6}$$

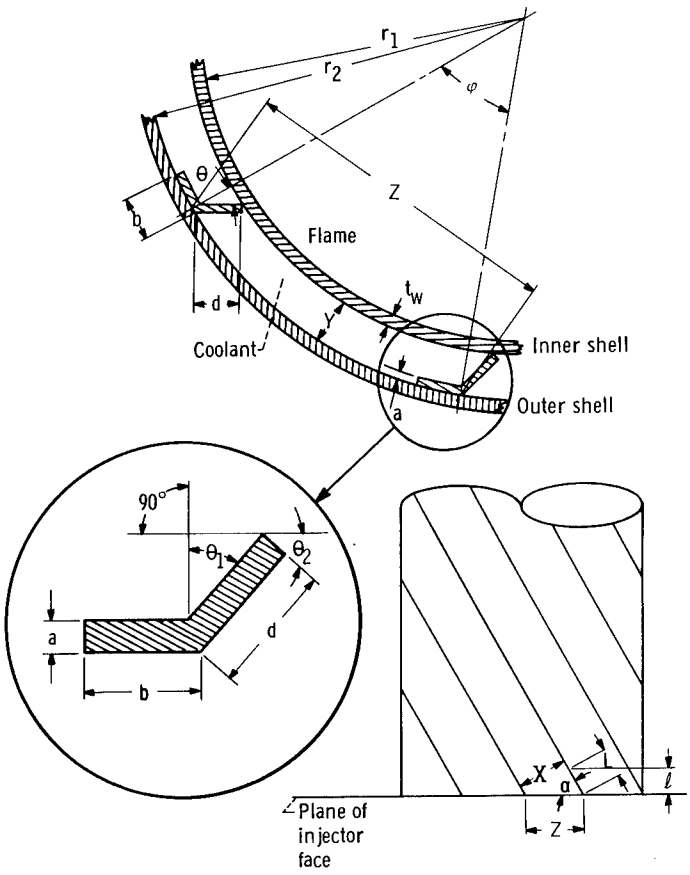

Figure 21. - Coolant passage geometry.

Thermal conductivity data for the 304 stainless steel wall was taken from reference 6 (p. 584).

Since the design was to consist of spiral passages, it was necessary to derive an expression relating the axial length to the coolant passage length or diameter. An alternate approach would establish the axial length as a function of the lead angle. For this design the latter approach was taken with

$$\ell = L \sin \alpha \tag{B7}$$

The lead angle α is shown in figure 21 and can also be expressed as

$$\alpha = \sin^{-1}\left(\frac{X}{Z}\right) \tag{B8a}$$

with

$$Z = 2(r_1 + t_w + Y) \sin \frac{360}{2N} \tag{B8b}$$

If spacers are used to obtain the coolant passages as shown in figures 4 and 21, the coolant passage area for one channel is

$$A_c = \frac{\pi(360/N)}{360} \left\{ \left[\frac{X/\sin \alpha}{2 \sin (360/2N)} \right]^2 - (r_1 + t_w)^2 \right\} \sin \alpha - \left[\left(b - a \tan \frac{90 - \theta}{2} \right) a + ad \right] \tag{B9}$$

Equation (B9) is derived in appendix D. The equivalent diameter or hydraulic diameter for one channel was taken as

$$D_e = \frac{4A_c}{\text{Wetted perimeter}} \tag{B10}$$

or in terms of the channel dimensions as

$$D_e = \frac{4A_c}{-\frac{a}{\sin (90 - \theta)} + \frac{\pi}{4} (2r_1 + 2t_w + d \cos \theta + a \sin \theta) + 2(a + d) - a \tan \frac{90 - \theta}{2} + a \tan \theta} \tag{B11}$$

The wetted perimeter as used in equation (B11) is derived in appendix D. The wall temperature on the coolant side established by equation (B6) and the given inlet temperature and pressure of the coolant were used to start iterations on the coolant side to establish the coolant passage geometry (channel widths as functions of axial length). Thus the coolant velocity necessary for a given weight flow to maintain the hot-side wall temperature at the design condition was established. The equations used were the following:

$$q = h_c(T_{w,c} - T_{c,b}) \tag{B12}$$

and

$$Nu_f = Re_f^{0.8} Pr_f^{0.4} \tag{B13}$$

which is the equation from reference 7 for subcritical pressure hydrogen gas vapor that is identical to equation (B3) for the combustion gas Nusselt number.

The heat-transfer coefficient h_c necessary to make the right-hand side of equation (B12) balance is readily determined from equation (B13) as

$$h_c = 0.023 \frac{k_f}{D_e} \left(\frac{W_c}{A_c} \frac{D_e}{g\mu_f} \right)^{0.8} \left(\frac{g\mu_f C_{p,f}}{k_f} \right)^{0.4} \tag{B14}$$

The film temperature for evaluation of physical properties in equation (B14) was defined as

$$T_{f,c} = 0.5(T_{w,c} + T_{c,b}) \tag{B15}$$

The interative procedure was started after arbitrarily dividing the engine axially into 11 increments. For the inlet (axial length equal to zero), h_c was established by assuming a value of channel width X and by using equations (B8a), (B8b), (B9), (B10), (B11), (B15), and (B14). If the value of the heat flux computed by equation (B12) did not agree with the heat flux computed by equation (B1), a new value of X was taken and the procedure repeated until satisfactory agreement with equation (B2) was obtained. When this condition was met, one increment axially was advanced and new trial state variables were calculated by using the following equations with the area A_c at the new station assumed equal to the area at iterative inlet:

$$Q = A_{sur} q = W_c C_{p,c,b} (T_{c,b,x} - T_{c,b,in}) \tag{B16}$$

$$V_{av} = \frac{W_c}{\rho_b A_c} \tag{B17}$$

$$P_{in} - P_x = \frac{W_c}{A_c g} \Delta V_{av} + \frac{2fL\rho_m V_{av}^2}{D_e g} \tag{B18}$$

with

$$\rho_m = \frac{m}{2R(1728)}\left(\frac{P_{in}}{T_{c,b,in}} + \frac{P_x}{T_{c,b,x}}\right) \tag{B19}$$

and

$$\frac{1}{\sqrt{f}} = 4 \log\left(Re\sqrt{f}\right) - 0.4 \tag{B20}$$

To obtain trial values of the state variables ($T_{c,b,x}$ and P_x), the pressure at station x is assumed equal to its value at station x - 1, and the temperature is calculated from equation (B16). When these values are used, the Reynolds number can then be determined. Thus, ρ_m and f can be calculated from equation (B19) and (B20), respectively. The velocity at X is then computed based on the assumed pressure from equation (B17). The coolant passage length L is computed from equation (B7) based on the previous value of α. With these variables known, a new P_x can be determined from equation (B18). The method to solve equation (B20) for f was to assume a value and iterate until the assumed value caused convergence.

The computed value of P_x was then used to repeat this procedure until successive calculations of P_x did not change. The values of $T_{c,b,x}$ and P_x computed thus become the state variables for computation of the new area A_c at station X. At this point, as with the inlet, the entire computational procedure is repeated starting again with equation (B8a) and terminating with equation (B18) until the heat flux computed by equation (B12) agrees with that computed by equation (1). Again one increment axially is advanced (of course the inlet conditions in eqs (16) and (19) are now conditions at the last condition X) until the entire length has been transversed. Because of the number of iterations involved, these equations and the procedure just described were programmed for solution on the IBM 7094 digital computer.

In the calculations of the pressure P_x at each axial station, the pressure drop per incremental length may be represented by

$$\frac{\Delta P}{\Delta L} = \text{Momentum losses} + \text{Frictional losses}$$

The frictional component is related to the wall shear stress, and its velocity and density are determined at a mixed or bulk temperature. This component is the second term on the right-hand side of equation (B18). The first term encompasses the momentum losses. Both pressure drop components are appreciable enough under the conditions imposed by this design, since the thermodynamic state of the coolant is a varying one which occasions

a substantial change in density as it proceeds along the length of the passage. The friction factor f in equation (B20) is from reference 8. It was also suggested in reference 7 for subcritical pressure hydrogen gas and vapor which is in the thermodynamic range of this design. Equation (B19) from reference 9(p. 350) is the nonisothermal mean density. The momentum loss term is from reference 10 and represents one-dimensional momentum change.

Figure 22 shows the result of the preceding design program. Coolant passage width for a coolant passage height of 0. 100 inch is given as a function of distance along the engine.

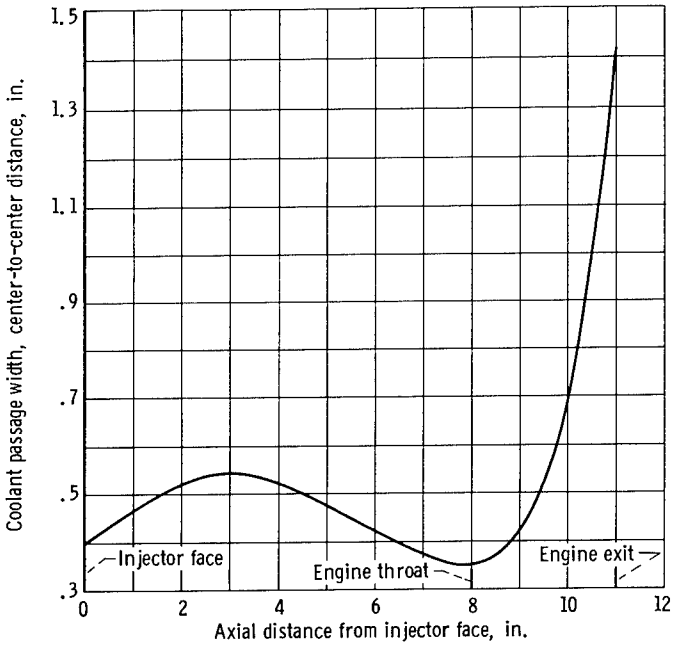

Figure 22. - Engine coolant passage design.

APPENDIX C

COOLANT PASSAGE PERFORMANCE PREDICTION

Subsequent to the design of the dump-cooled engine, it was established that the coolant hydrogen would enter the engine at 85° R and at pressures ranging from 90 to 140 psia instead of at 57° R and 150 psia as originally assumed. Furthermore, improved transport properties for the combustion gases (ref. 2) became available and allowed an improvement of the theoretical heat-flux distribution.

As part of the evaluation procedure, a distribution of the theoretical heat flux across the engine was introduced into the analytical program. The heat flux is a function of the hot-side wall temperature, which was established as an upper limit (consistent with wall material and thickness) and predicated upon a specific propellant combination, mass flow rate, and chamber pressure.

When an off-design situation was assumed, an envelope of static pressure and temperature along the coolant passages was developed from an evaluation for a given coolant mass flow at a specified inlet temperature and pressure. The envelope was consistent with the theoretical heat flux introduced into the program. This involved an iteration. Since the coolant passage geometry is fixed, the heat flux through the wall is balanced by the heat absorbing capability of the coolant hydrogen for each station taken along its length. Conceivably, for a particular station the coolant may not possess the capability to reduce the wall temperature below the established upper limit. The analysis would indicate this as a burnout location.

The heat absorbing capability of the coolant as measured by the heat-transfer coef-

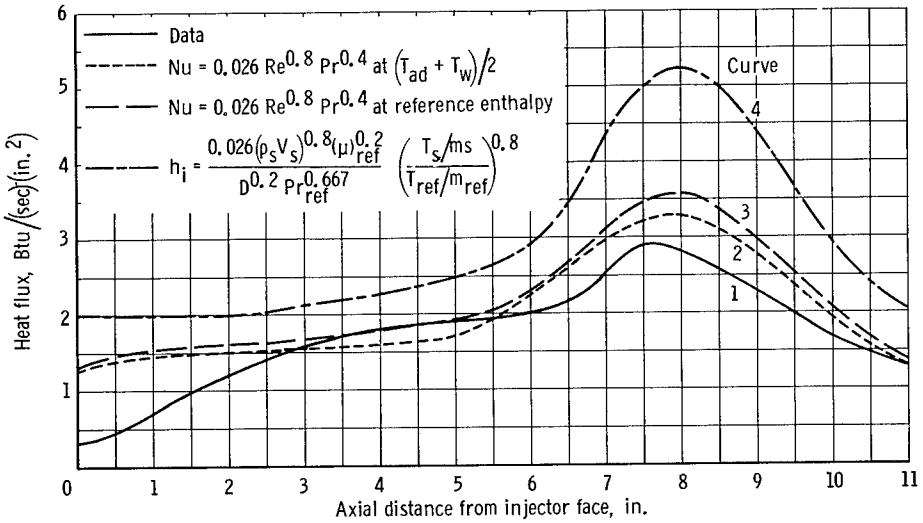

Figure 23. - Heat flux distribution along length of engine for firing 9.

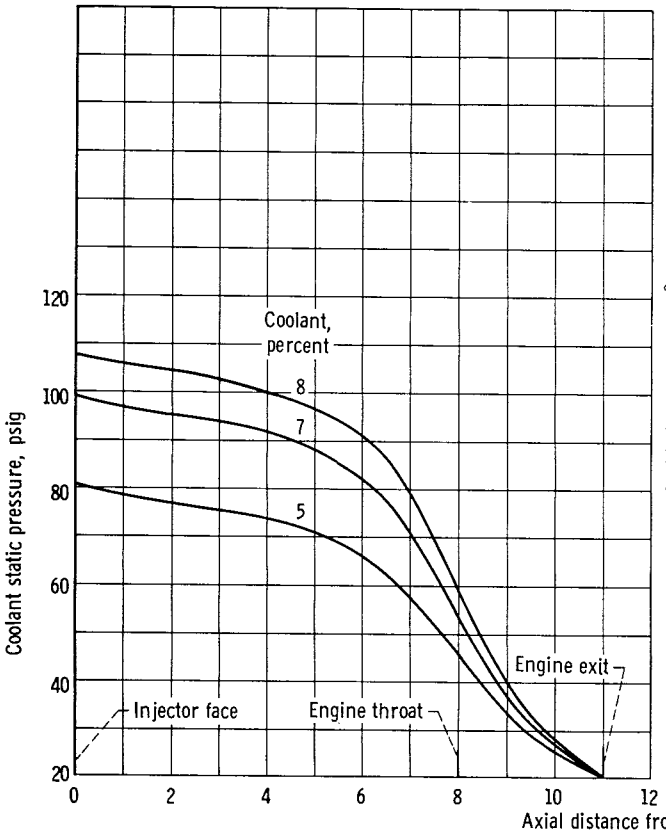

(a) Effect of coolant flow (percent of total propellants) on coolant static pressure distribution.

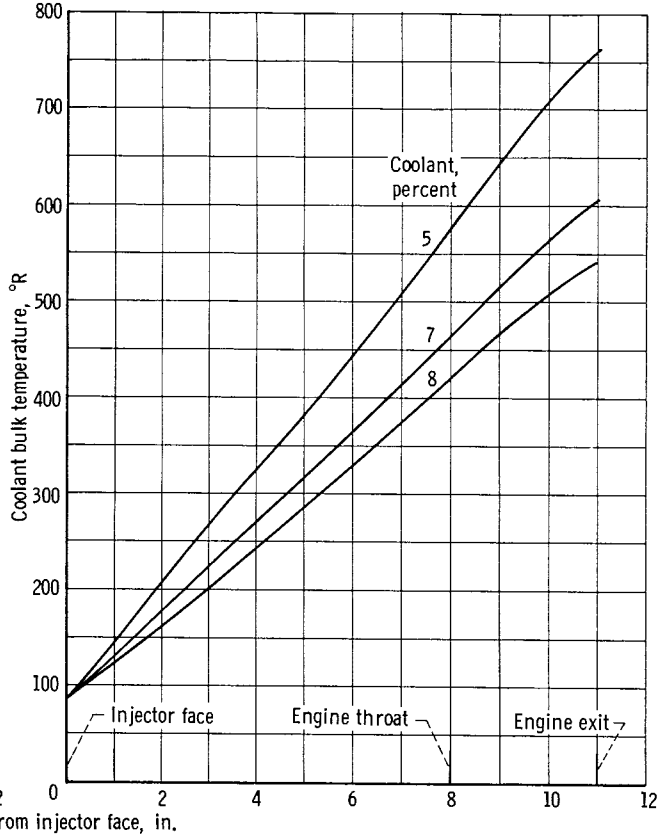

(b) Effect of coolant flow (percent of total propellants) on coolant bulk temperature distribution.

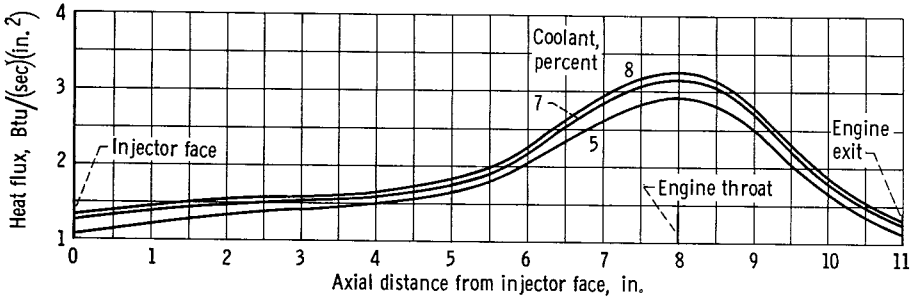

(c) Effect of coolant flow (percent of total propellants) on heat flux distribution.

Figure 24. - Predicted coolant performance. Mixture ratio, 3.2; coolant inlet temperature, 85.9° R.

ficient is expressed by equation (B14) in appendix B and is a part of the evaluation routine. If the coolant has greater capacity than the heat flux for the specified hot-side wall temperature, the iteration proceeds to adjust the heat flux and the wall temperatures and defines the thermodynamic state of the coolant for the next station.

In regard to ascertaining the theoretical heat flux for the analytical procedure, three different criteria are presented in figure 23 along with the data derived from test firing 9. Curve 4 with the greatest heat flux along the length of the engine is outlined in reference 11. In this regard, the one-dimensional approach for the mass velocity determination was used throughout for this calculation. Curve 3 follows the correlation outlined in reference 12 with a slight modification. For the constant B a value of 0.026 was used throughout instead of the range of values presented. This decision would appear reasonable in view of the low chamber pressure and Reynolds number of 0.275×10^6 at the throat for the dump-cooled engine. A further adjustment in the exponent of the Prandtl number showed better agreement with the data curve in figure 23. Curve 3 is similar to the simplified Bartz equation of reference 13. Curve 2 in the same figure evaluates combustion transport properties at the mean temperature between flame-side adiabatic wall temperature and actual hot-side wall temperatures. This procedure is the basis for the analytical curves included on the plots of experimental results and figure 24 which typified the output of this evaluation.

APPENDIX D

COOLANT PASSAGE GEOMETRY

For engines of this size (see fig. 3) and larger, the difference between θ_1 and θ_2 is negligible, so $\theta_1 = \theta_2 = \theta$ (see fig. 21). The following describe the coolant flow area A_c of one coolant passage:

$$\text{Small radius} = r_1 + t_w \tag{D1}$$

$$\text{Large radius} = r_2 = r_1 + t_w + Y \tag{D2}$$

$$Z = 2(r_1 + t_w + Y) \sin \frac{360}{2N} = \frac{x}{\sin \alpha} \tag{D3}$$

$$Y = d \cos \theta + a \sin \theta \tag{D4}$$

$$A_a = \frac{\pi\varphi \left[r_2^2 - (r_1 + t_w)^2\right]}{360} \tag{D5}$$

$$\varphi = \frac{360}{N} \tag{D6}$$

From equation (D2) and (D3),

$$r_2 = (r_1 + t_w + Y) = \frac{Z}{2 \sin (\varphi/2)} = \frac{X/\sin \alpha}{2 \sin (\varphi/2)} \tag{D7}$$

Substituting r_2 into equation (D5) gives

$$A_a = \frac{\varphi\pi}{360} \left\{ \left[\frac{X/\sin \alpha}{2 \sin (\varphi/2)} \right]^2 - (r_i + t_w)^2 \right\} \tag{D8}$$

$$A_c = A_a \sin \alpha - \text{Area of spacers} \tag{D9}$$

$$\text{Area of spacers} = \left[b - a \tan \left(\frac{90^\circ - \theta}{2} \right) \right] a + ad \tag{D10}$$

Therefore,

$$A_c = \left(\frac{\pi(360/N)}{360} \left\{ \left[\frac{X/\sin \alpha}{2 \sin (360/2N)} \right]^2 - (r_i + t_w)^2 \right\} \right) \sin \alpha - \left[\left(b - a \tan \frac{90^o - \theta}{2} \right) a + ad \right] \tag{D11}$$

The equivalent diameter is defined as

$$D_e = \frac{4A_c}{\text{Wetted perimeter}} \tag{D12}$$

In figure 21 the circumferences for both large and small radii per sector are given as

$$\left(\frac{c}{N}\right)_2 = \left(\frac{c}{8}\right)_2 2\pi(r_1 + t_w + Y) \tag{D13}$$

$$\left(\frac{c}{N}\right)_1 = \left(\frac{c}{8}\right)_1 = 2\pi(r_1 + t_w) \tag{D14}$$

The wetted perimeter is

$$\text{Wetted perimeter} = \left(\frac{c}{8}\right)_2 + \left(\frac{c}{8}\right)_1 + 2a + d - a \tan \frac{90^o - \theta}{2} + \frac{Y}{\cos \theta} - \frac{a}{\sin (90^o - \theta)} \tag{D15}$$

Substituting yields

$$\text{Wetted perimeter} = \frac{\pi}{4}(2r_i + 2t_w + d \cos \theta + a \sin \theta) + 2(a + d) - a \tan \frac{90^o - \theta}{2} + a \tan \theta - \frac{a}{\sin (90^o - \theta)} \tag{D16}$$

APPENDIX E

DATA COLLECTION

Tabulated herein are the coolant temperatures and pressures measured at the 18 pressure tap locations and 18 thermocouple locations shown in figure 7.

These were measured during steady-state conditions (last 3 sec of the 10-sec firings) for each of the 14 firings.

TABLE II. - EXPERIMENTAL DATA

[Nominal chamber pressure, 100 psig.]

(a) Coolant static pressure

Firing	Mixture ratio, O/F	Coolant flow, W_c, lb/sec	Coolant, $\frac{W_c}{W_o + W_F} \times 100$, percent	Coolant static pressure taps																
				1	2	3	4	5	6	7	8	9	10	11	12	13	14	15	16	17	18
				Static pressure, psig																	
1	2.27	0.179	11.4	128.9	128.6	122.7	119.6	115.5	110.3	102.3	99.5	61.4	66.6	90.8	78.9	77.8	61.5	82.9	79.1	22.0	22.2
2	3.21	.162	9.5	132.8	131.8	125.7	123.5	118.8	114.2	107.0	103.5	63.7	69.7	95.9	83.5	81.6	65.8	85.3	82.5	21.7	21.6
3	2.76	.149	9.4	110.8	109.5	103.9	101.7	98.2	94.2	88.8	83.8	51.8	63.1	68.5	69.8	63.7	52.3	65.0	66.1	18.6	18.5
4	3.48	.153	8.6	125.7	124.5	119.8	117.6	113.5	108.9	102.8	97.9	60.5	66.8	91.5	79.2	77.3	62.0	80.8	77.9	20.0	19.7
5	5.44	.148	8.3	119.7	118.3	115.6	115.2	111.7	108.5	104.8	100.4	63.1	80.5	91.9	81.8	80.2	76.6	84.6	78.2	20.8	20.2
6	3.21	.129	7.7	113.0	111.6	106.5	104.4	100.0	96.6	91.9	88.2	54.0	69.7	78.6	74.5	67.4	59.4	72.3	68.6	17.6	17.8
7	3.57	.136	7.7	111.8	110.4	105.8	104.7	100.9	97.2	109.8	86.9	54.5	58.8	80.8	68.9	67.7	63.0	73.9	68.1	17.7	17.0
8	4.84	.142	7.8	114.4	114.8	111.8	110.5	108.5	105.5	102.1	97.1	89.8	74.0	85.9	77.9	76.6	71.4	78.7	73.5	18.4	17.9
9	5.01	.142	7.8	121.4	119.8	116.9	115.9	112.5	108.9	104.6	99.1	62.9	74.2	91.8	80.7	78.5	74.1	84.4	77.8	20.6	19.9
10	4.97	.137	7.5	110.4	110.8	107.8	106.7	104.7	101.8	98.5	94.4	86.6	74.2	82.9	80.4	74.9	66.8	75.7	72.7	17.3	16.9
11	5.01	.174	9.7	87.9	88.1	86.4	86.1	84.5	82.6	78.0	74.6	67.9	64.5	61.1	60.5	55.1	55.0	57.6	62.0	20.5	20.2
12	5.46	.133	7.5	93.2	93.1	92.8	92.2	90.8	89.2	87.0	84.1	80.6	76.1	79.3	78.1	69.4	59.5	70.4	75.6	15.5	15.4
13	5.35	.125	6.9	87.3	87.5	86.3	85.4	84.4	83.3	80.4	77.4	74.0	69.8	73.9	70.6	63.3	56.9	63.5	68.8	14.4	14.3
14	5.25	.120	6.9	80.5	80.5	78.7	78.0	77.5	74.7	70.3	66.4	58.8	58.5	61.7	57.5	50.9	42.1	51.5	57.2	14.5	14.3

(b) Coolant bulk temperature

Firing	Mixture ratio, O/F	Coolant flow, W_c, lb/sec	Coolant, $\frac{W_c}{W_o + W_F} \times 100$, percent	Thermocouple number																
				1	2	3	4	5	6	7	8	9	10	11	12	13	14	15	16	17	18
				Temperature, ^{o}R																	
1	2.27	0.179	11.4	86.0	83.5	104.0	143.4	-----	266.0	266.0	345.0	368.6	-----	337.8	373.0	335.5	372.2	417.5	390.8	417.5	417.0
2	3.21	.162	9.5	87.0	84.8	104.0	131.0	-----	275.5	274.0	361.0	395.8	366.0	359.0	403.0	362.0	409.0	449.0	448.0	449.0	444.0
3	2.76	.149	9.4	73.0	74.5	110.5	172.6	-----	187.5	385.7	381.5	439.4	406.0	398.0	462.0	456.5	437.5	461.7	441.0	535.0	489.0
4	3.48	.153	8.6	86.6	84.3	102.0	149.5	-----	290.5	295.5	384.0	406.5	387.5	386.0	426.0	366.0	405.0	465.0	433.3	470.0	473.0
5	5.44	.148	8.3	77.8	77.8	114.5	185.5	-----	272.0	318.2	366.0	485.5	413.0	410.5	453.5	456.5	455.0	469.0	472.0	521.3	524.0
6	3.21	.129	7.7	75.8	73.7	100.8	155.1	-----	326.0	396.2	445.0	501.8	444.5	462.8	537.0	513.9	541.7	519.0	508.0	478.8	540.0
7	3.57	.136	7.7	76.8	75.7	135.0	-----	-----	335.0	415.0	-----	542.5	483.0	485.0	452.3	436.0	479.0	579.0	572.0	-----	587.5
8	4.84	.142	7.8	74.5	74.5	115.0	189.5	-----	313.0	342.0	399.5	515.0	426.0	427.0	477.5	-----	463.5	515.0	517.0	552.4	546.3
9	5.01	.142	7.8	77.0	77.2	148.0	170.0	-----	275.0	339.0	367.5	469.0	394.0	420.0	435.5	465.0	434.5	495.4	491.0	526.0	525.0
10	4.97	.137	7.5	73.5	74.5	115.6	174.5	-----	337.0	366.0	450.0	530.0	451.3	456.5	513.0	485.3	465.0	503.0	538.0	567.0	571.5
11	5.01	.174	9.7	76.2	78.6	79.6	103.5	-----	166.5	217.5	232.5	287.5	285.0	321.5	281.0	268.5	261.0	252.5	290.6	343.0	347.0
12	5.46	.133	7.5	77.8	79.6	88.3	102.3	-----	259.0	279.0	290.5	341.0	322.6	378.6	322.4	343.0	346.5	321.0	337.5	450.1	449.7
13	5.35	.125	6.9	78.5	80.0	99.0	111.2	-----	272.0	277.0	301.5	357.5	385.6	375.5	333.6	358.5	387.0	340.0	380.2	469.1	467.2
14	5.25	.120	6.9	74.0	80.7	108.0	157.5	-----	239.5	286.5	362.0	458.0	426.0	456.0	413.0	403.0	398.5	381.0	420.0	525.0	525.0

REFERENCES

1. Gordon, Sanford; and McBride, Bonnie J.: Theoretical Performance of Liquid Hydrogen with Liquid Oxygen as a Rocket Propellant. NASA Meo 5-21-59E, 1959.
2. Svehla, Roger A.: Thermodynamic and Transport Properties for the Hydrogen-Oxygen System. NASA SP-3011, 1964.
3. Hsu, Shao-Ti: Engineering Heat Transfer. D. Van Nostrand Co., Inc., Dec. 1963.
4. Curren, Arthur N.; Price, Harold G., Jr.; and Douglass, Howard W.: Analysis of Effects of Rocket-Engine Design Parameters on Regenerative-Cooling Capabilities of Several Propellants. NASA TN D-66, 1959.
5. Eckert, Ernst R. G.: Introduction to the Transfer of Heat and Mass. 1st ed., McGraw-Hill Book Co. Inc., 1950, pp. 150-158.
6. Brown, George G.; et al: Unit Operations. John Wiley and Sons, Inc., 1950.
7. Hendricks, R. C.; Graham, R. W.; Hsu, Y. Y.; and Medeiros, A. A.: Correlation of Hydrogen Heat Transfer in Boiling and Supercritical Pressure States. ARS J., vol. 32, no. 2, Feb. 1962, pp. 244-252.
8. McAdams, William H.: Heat Transmission. 3rd ed., McGraw-Hill Book Co., Inc., 1964.
9. Dodge, Barnett F.: Chemical Engineering Thermodynamics. McGraw-Hill Book Co., Inc., 1944.
10. Hendricks, R. C.; Graham, R. W.; Hsu, Y. Y.; and Friedman, R.: Experimental Heat Transfer and Pressure Drop of Liquid Hydrogen Flowing Through a Heated Tube. NASA TN D-765, 1961.
11. Benser, W. A.; and Graham, R. W.: Hydrogen Convective Cooling of Rocket Nozzles. Paper No. 62-AV-22, ASME, June 1962.
12. Schacht, Ralph L.; Quentmeyer, Richard J.; and Jones, William L.: Experimental Investigation of Hot-Gas Side Heat-Transfer Rates for a Hydrogen-Oxygen Rocket. NASA TN D-2832, 1965.
13. Bartz, D. R.: A Simple Equation for Rapid Estimation of Rocket Nozzle Convective Heat Transfer Coefficients. Jet Propulsion, vol. 27, no. 1, Jan. 1957, pp. 49-51.

"The aeronautical and space activities of the United States shall be conducted so as to contribute . . . to the expansion of human knowledge of phenomena in the atmosphere and space. The Administration shall provide for the widest practicable and appropriate dissemination of information concerning its activities and the results thereof."

—NATIONAL AERONAUTICS AND SPACE ACT OF 1958

NASA SCIENTIFIC AND TECHNICAL PUBLICATIONS

TECHNICAL REPORTS: Scientific and technical information considered important, complete, and a lasting contribution to existing knowledge.

TECHNICAL NOTES: Information less broad in scope but nevertheless of importance as a contribution to existing knowledge.

TECHNICAL MEMORANDUMS: Information receiving limited distribution because of preliminary data, security classification, or other reasons.

CONTRACTOR REPORTS: Technical information generated in connection with a NASA contract or grant and released under NASA auspices.

TECHNICAL TRANSLATIONS: Information published in a foreign language considered to merit NASA distribution in English.

TECHNICAL REPRINTS: Information derived from NASA activities and initially published in the form of journal articles.

SPECIAL PUBLICATIONS: Information derived from or of value to NASA activities but not necessarily reporting the results of individual NASA-programmed scientific efforts. Publications include conference proceedings, monographs, data compilations, handbooks, sourcebooks, and special bibliographies.

Details on the availability of these publications may be obtained from:

SCIENTIFIC AND TECHNICAL INFORMATION DIVISION

NATIONAL AERONAUTICS AND SPACE ADMINISTRATION

Washington, D.C. 20546